Engineering Journal

Fourth Quarter 2025 | Volume 62, No. 4

AISC

Smarter.
Stronger.
Steel.

Steel Structures Research Update

Engineering Journal

American Institute of Steel Construction

Dedicated to the development and improvement of steel construction, through the interchange of ideas, experiences, and data.

Editorial Staff

Editor	Margaret A. Matthew, PE
Managing Editor	Keith A. Grubb, SE, PE
Research Editor	Judy Liu, PhD
Production Editor	Kristin Hall

Officers

Chair
Glenn R. Tabolt, PE

Vice Chair
Dan Kadrmas

Secretary/Legal Counsel
Edward Seglias

President
Charles J. Carter, SE, PE, PhD

Senior Vice Presidents
Scott L. Melnick
Mark W. Trimble, PE

Vice Presidents
Todd Alwood
Brandon Chavel, PE, PhD
Carly Hurd, CAE
Christopher H. Raebel, SE, PE, PhD
Brian Raff

The articles contained herein are not intended to represent official attitudes, recommendations or policies of the Institute. The Institute is not responsible for any statements made or opinions expressed by contributors to this Journal.

The opinions of the authors herein do not represent an official position of the Institute, and in every case the officially adopted publications of the Institute will control and supersede any suggestions or modifications contained in any articles herein.

The information presented herein is based on recognized engineering principles and is for general information only. While it is believed to be accurate, this information should not be applied to any specific application without competent professional examination and verification by a licensed professional engineer. Anyone making use of this information assumes all liability arising from such use.

Manuscripts are welcomed, but publication is not guaranteed. Authors do not receive a remuneration. *Engineering Journal* (ISSN 0013-8029) is published quarterly. Published by the American Institute of Steel Construction at 130 E Randolph Street, Suite 2000, Chicago, IL 60601.

Copyright 2025 by the American Institute of Steel Construction. All rights reserved. No part of this publication may be reproduced without written permission. The AISC logo is a registered trademark of AISC.

The Chevron Effect Further Demystified through the Lower Bound Theorem

PATRICK S. MCMANUS and JAY PUCKETT

ABSTRACT

The transfer of brace forces at braced frame connections in V, inverted-V, and X brace configurations is discussed. Force transfer under these configurations considers both wide-flange (WF) and rectangular hollow structural sections (HSS) for the horizontal beam or strut. The analogous condition of truss web-to-chord connections using gusset plates is discussed. Analogies are expanded to address the condition of beam-to-column brace connections using a common gusset plate to receive the horizontal beam/strut and braces above and below the beam/strut. The potential to redistribute forces using the assumptions of the lower bound theorem is investigated. Additionally, the transposition of shear forces to axial forces in connections at X-brace configurations is illustrated. In conclusion, several methods can address the transfer of brace forces in gusset plate connections. Shear forces in the beam/strut, truss chord, or column members for the various conditions can be reduced by redistributing forces to properly proportioned gusset plates using the assumptions of the lower bound theorem. A reduction in shear forces in the primary members can effectively avoid localized member reinforcement, such as doubler plates or upsizing of members.

Keywords: chevron effect, braced frame connections, lower bound theorem, Uniform Force Method.

INTRODUCTION

Several methods have been presented in recent years to address the force transfer at the intersection of beams and braces in V and inverted-V (chevron) braced frame configurations (Fortney and Thornton, 2015, 2017; Sabelli et al., 2021; Sabelli and Saxey, 2023). Traditionally, the methodology used at V and inverted-V configurations has been applied to super-X (also known as two-story X) configurations by assuming the super-X has a V configuration above the beam and an inverted-V below the beam (see Figure 1). Differences between the behaviors are discussed herein. Alternative methods for addressing the force transfer of each condition are presented.

V AND INVERTED-V BRACE CONNECTIONS

Figure 2 illustrates a free-body diagram (FBD) of a typical inverted-V connection where the story shear A_b is resisted by two brace forces *P,* one in compression and the other in tension. The associated directional forces are represented with *V* and *H* for vertical and horizontal force components, respectively. Previous work has shown that concentrically detailed braces in V and inverted-V configurations produce shears in the beam and gusset plate assembly between the brace attachment points, a phenomenon known as the "chevron effect" (Fortney and Thornton, 2015). Under an elastic analysis, a portion of the shear resulting from the vertical components of the brace force, *V*, as illustrated in Figure 2, is distributed to the beam based on the relative stiffness of the beam to the stiffness of the beam and gusset-plate assembly. The remaining portion of the shear is transferred within the gusset plate. Gravity load effects are neglected herein to simplify the discussion.

Axial shortening and lengthening of the braces in compression and tension results in a story drift and a localized rotation in the beam at the interface with the brace connections. Assumed force distributions and neglect of incidental forces associated with frame deformations in connection design are made possible by implementing the lower-bound theorem (LBT). The LTB is discussed in numerous texts addressing plastic solid mechanics (e.g., Bower, 2010; Barker and Puckett, 2021) and has the following three fundamental attributes as it relates to steel connection design:

1. An assumed load path that satisfies static equilibrium.
2. Sufficient capacity for all limit states associated with the assumed load path.
3. Adequate ductility to allow for force redistribution to the assumed load path (i.e., detailing for inelastic behavior).

Traditionally, steel connection design is performed through a force-based approach using the LBT rather than

---

Patrick S. McManus, PE, SE, PhD, Principal, Martin/Martin Consulting Engineers, Cheyenne, Wyo. Email: pmcmanus@martinmartin.com (corresponding author)

Jay Puckett, PE, PhD, Principal, Novel Structures, LLC, Cheyenne, Wyo. Email: jay.a.puckett@novelstructures.com

Paper No. 2024-03R

a stiffness-based approach. In some cases, certain rules or limitations may be applied to ensure acceptable ductility. The Uniform Force Method (UFM) for the design of braced-frame connections, as presented in the AISC *Steel Construction Manual* (2023), hereafter referred to as the AISC *Manual*, is an example of such a force-based approach. The fundamental assumption of ductility under this method allows for the redistribution of forces, such as that of redistributed shear forces under Special Case 2 as illustrated in the AISC *Manual*. By applying the LBT to V and inverted-V connections, it can be recognized that yielding within the beam is not detrimental to the desired behavior, or performance, provided all limit states associated with an assumed load path are adequately addressed.

Two fundamental force transfer models bound the required shear the beam must carry in a concentric V or inverted-V brace configuration. The first assumes that each brace's axial force is transferred into and out of the beam in its entirety. The second assumes a continuous gusset transfers the entirety of the vertical shear such that only horizontal components of brace forces need to be transferred into the beam. The first approach effectively discounts any contribution of the gusset in resisting the vertical shear and is consistent with the required force transfer in a discontinuous gusset condition as illustrated in Figure 3. This approach is common where brace angles measured from horizontal are shallow and/or at deep beams. In these conditions, the use of separate gusset plates for each brace-to-beam connection can avoid an excessively long, continuous gusset plate. Under this force transfer assumption, the geometry of the welds for each gusset plate can be balanced about each workline to avoid any eccentricity on the weld. Alternatively, the weld geometry can deviate from a concentric condition provided the moments due to any eccentricity are considered.

Where gusset plates are made continuous between braces, the opportunity exists to utilize the vertical shear capacity of the gusset plate to reduce the vertical shear from

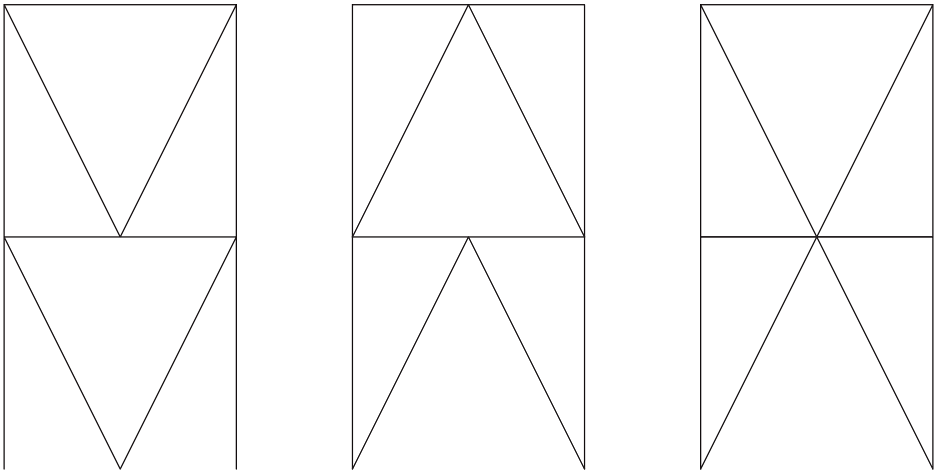

(a) Stacked V *(b) Stacked inverted V* *(c) Super X*

Fig. 1. Typical braced-frame configurations.

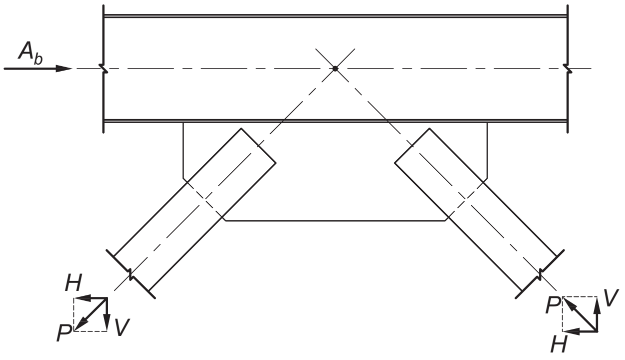

Fig. 2. Inverted-V brace configuration force transfer at connection.

the braces theoretically transferred to the beam. Figure 4 shows a force distribution generally consistent with Special Case 2 of the UFM, whereby a portion of the vertical shear, ΔV_b, can be redistributed to the gusset plate to reduce the shear in the beam as long as the resulting force actions—namely, M_g—are considered to provide equilibrium. At one extreme, ΔV_b can be set equal to V, thereby eliminating assumed shear to the beam due to the vertical component of the brace forces as long as the connection between the gusset plate and beam accounts for the horizontal shear, $2H$, and the moment $M_g = \Delta V_b L_{\text{wl}}$, which, in this case, becomes equal to $2Hd_b/2 = A_b d_b/2$. Though nomenclature differs, these forces are consistent with those illustrated in Figures 4, 5, and 6 of AISC Design Guide 29, assuming braces with balanced forces at equal angles of inclination (Muir and Thornton, 2014). As noted by Fortney and Thornton (2015), the force distribution becomes more complicated with the addition of gravity loads, unequal brace angles, and/or unbalanced loads, though the general theory remains unchanged.

As an example, assume the condition shown in Figure 4 with the following attributes where all loads are assumed factored using load and resistance factor design (LRFD):

Beam = W18×40 ASTM A572/A572M Gr. 50 (ASTM, 2021)
Braces = HSS8×8×⅜ oriented at 45° angles from horizontal ASTM A500/A500M Gr. C (ASTM, 2023)
Gusset plate thickness = ½ in. (ASTM A572/A572M Gr. 50)
$L_g = 50$ in.
$d_g = 14$ in.
$A_b = 400$ kips

Therefore, $P = 283$ kips and $H = V = 200$ kips.

The available LRFD shear strength of the beam is determined using AISC *Specification* Equation G2-1:

$$\begin{aligned}\phi R_n &= \phi 0.6 F_y A_w C_{v1} \qquad (1)\\ &= 1.0(0.6)(50\text{ ksi})(0.315\text{ in.})(17.9\text{ in.})(1.0)\\ &= 169\text{ kips}\end{aligned}$$

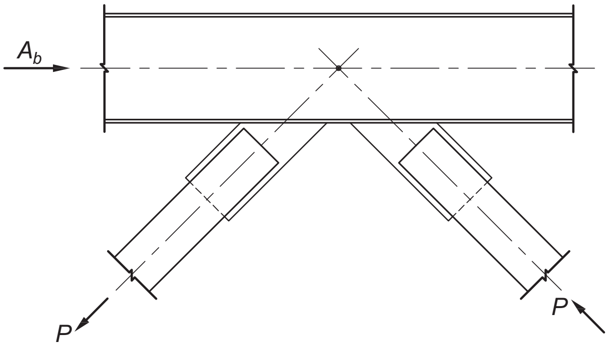

Fig. 3. Inverted-V connection with discontinuous gusset.

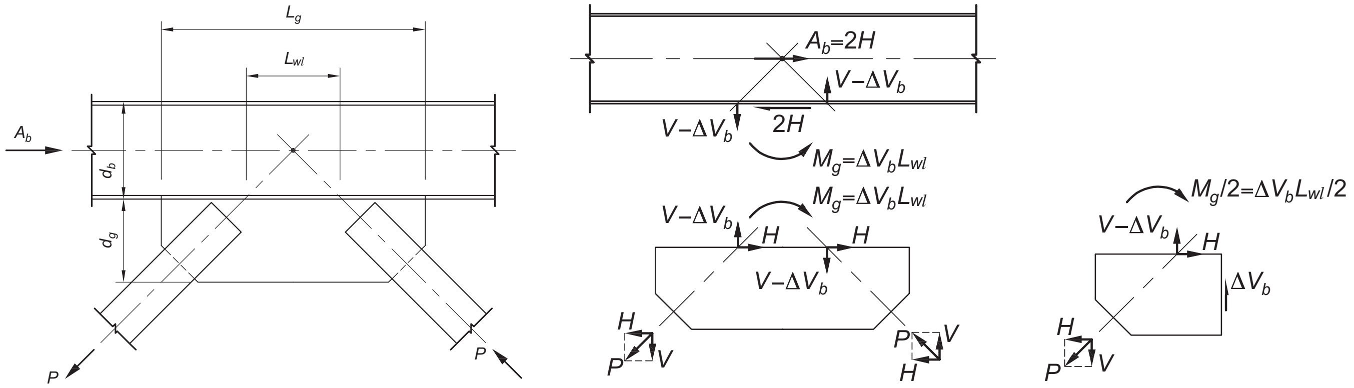

(a) Connection assembly

(b) FBD illustrating load transfer

(c) Left half of the gusset plate

Fig. 4. Inverted-V brace configuration force transfer.

Therefore, for the limit state of shear yielding, the beam alone is insufficient to resist the vertical shear, *V*, of 200 kips. This can be illustrated clearly through finite element analysis (FEA) of the example configuration, but with the gusset made discontinuous similar to the configuration shown in Figure 3, which mandates the distribution of all vertical shear to the beam. Force-controlled FEA was performed using Comsol Multiphysics® software (2023). Partial models (joint only), such as those used in an attempt to reflect a system's overall behavior, can be sensitive to boundary conditions. To best address this issue, the models herein incorporate a 15-ft floor-to-floor height and 30-ft column-to-column spacing. The full length of beams and braces were included in the models, each with pinned ends, to adequately capture the influence of member axial, flexural, and shear stiffness. Nonlinear material characteristics were implemented to allow for inelastic behavior. An example of a model is shown in Figure 5.

Figure 6 shows substantial yielding in the shear region between gusset plates with large shear deformation due to inelastic strains. By calculation, an average shear stress of 59 ksi is required across the full depth of the beam to resist the applied shear. The nonlinear FEA model allowed for strain hardening and was able to achieve static equilibrium at stresses of approximately 60 ksi uniformly spread across the region between gusset plates consistent with the calculated requirement, the difference likely due to the minimal contribution of brace flexure. The large inelastic strains resulting from failure of the yield criterion are unacceptable for a connection intended to behave substantially elastic under the applied loading.

By making the gusset plate continuous consistent with the intended configuration shown in Figure 4, the required shear can be redistributed to the gusset plate. Assuming the entire required vertical shear is distributed to the gusset plate as discussed previously, the required vertical shear in the beam becomes zero. The LRFD forces associated with this assumption are as follows:

$$\begin{aligned}\Delta V_b &= V = 200 \text{ kips}\\ 2H &= A_b = 400 \text{ kips}\\ M_g &= 2H\frac{d_b}{2} \qquad (2)\\ &= (400 \text{ kips})\frac{(17.9 \text{ in.})}{2}\\ &= 3{,}580 \text{ kip-in.}\end{aligned}$$

Per AISC *Specification* Equations J4-3 and J4-4 for shear yielding and shear rupture, respectively, the available LRFD shear strengths of the gusset plate along a vertical plane are determined as:

$$\begin{aligned}\phi R_{n-yield} &= \phi 0.6 F_y A_{gv} \qquad (3)\\ &= 1.0(0.6)(50 \text{ ksi})(0.5 \text{ in.})(14 \text{ in.})\\ &= 210 \text{ kips} > 200 \text{ kips} \quad \textbf{o.k.}\end{aligned}$$

$$\begin{aligned}\phi R_{n-rupture} &= \phi 0.6 F_u A_{nv} \qquad (4)\\ &= 0.75(0.6)(65 \text{ ksi})(0.5 \text{ in.})(14 \text{ in.})\\ &= 204 \text{ kips} > 200 \text{ kips} \quad \textbf{o.k.}\end{aligned}$$

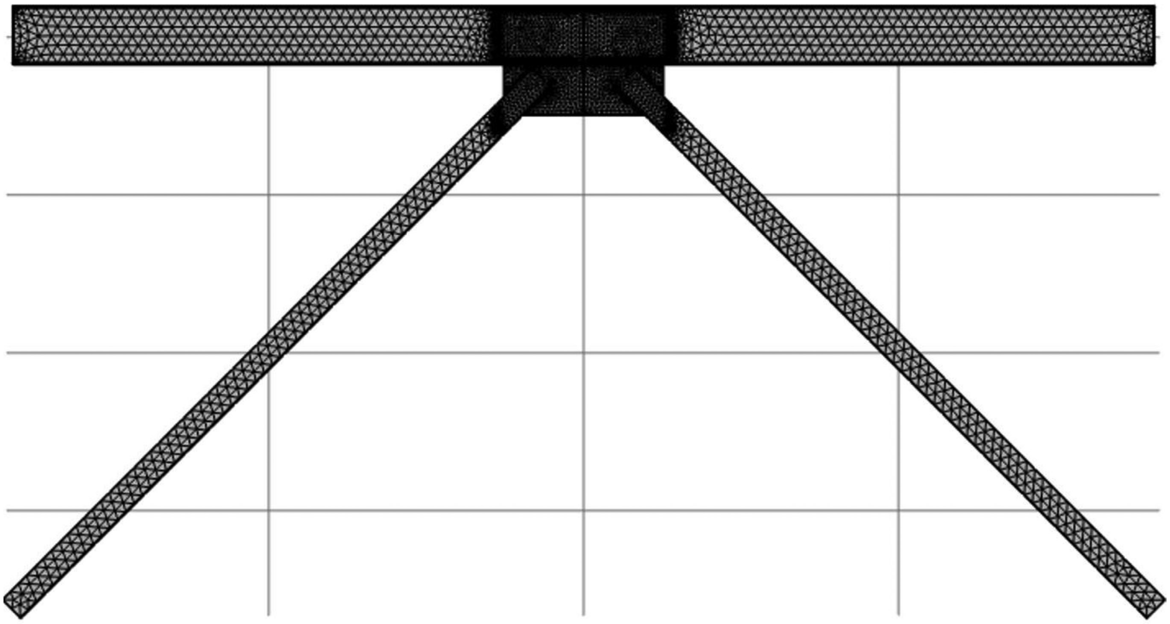

Fig. 5. Example inverted-V brace configuration FEA model.

Per AISC *Specification* Equations J4-3 and J4-4 for shear yielding and shear rupture, respectively, the available LRFD shear strengths of the gusset plate along a horizontal plane at the interface with the beam is determined as:

$$\begin{aligned}\phi R_{n-yield} &= \phi 0.6 F_y A_{gv} \\ &= 1.0(0.6)(50\text{ ksi})(0.5\text{ in.})(50\text{ in.}) \\ &= 750\text{ kips}\end{aligned} \tag{5}$$

$$\begin{aligned}\phi R_{n-rupture} &= \phi 0.6 F_u A_{nv} \\ &= 0.75(0.6)(65\text{ ksi})(0.5\text{ in.})(50\text{ in.}) \\ &= 729\text{ kips (governs)}\end{aligned} \tag{6}$$

The plastic LRFD flexural strength of the gusset plate along the interface with the beam is determined as:

$$\begin{aligned}\phi M_{n-yield} &= \phi F_y Z_g \\ &= 0.9(50\text{ ksi})\frac{(0.5\text{ in.})(50\text{ in.})^2}{4} \\ &= 14{,}060\text{ kip-in. (governs)}\end{aligned} \tag{7}$$

$$\begin{aligned}\phi M_{n-rupture} &= \phi F_u Z_n \\ &= 0.75(65\text{ ksi})\frac{(0.5\text{ in.})(50\text{ in.})^2}{4} \\ &= 15{,}230\text{ kip-in.}\end{aligned} \tag{8}$$

The interaction for planar stresses on the gusset plate is determined using AISC *Manual* Equation 9-1:

$$\begin{aligned}\frac{M_r}{M_c}+\left(\frac{P_r}{P_c}\right)^2+\left(\frac{V_r}{V_c}\right)^4 &= \frac{3{,}580\text{ kip-in.}}{14{,}060\text{ kip-in.}}+\left(\frac{400\text{ kips}}{729\text{ kips}}\right)^4 \\ &= 0.346 < 1.0 \quad \textbf{o.k.}\end{aligned} \tag{9}$$

The remaining checks are for the beam web and are discussed in detail later.

Though the vertical component of the brace force has been resolved into the gusset, the presence of a moment on the gusset-to-beam interface signifies there is still an unavoidable state of shear stress in the beam. The same is true when using AISC *Manual* Special Case 2. The redistribution of the shear from the shear connection to the gusset-to-column connection eliminates shear resulting from the force in the brace on the beam connection. However, the moment imposed on the gusset-to-beam interface resulting from the redistribution of shear must be resisted by a portion of the beam web, but at a location slightly away from the beam connection. The location and magnitude of the shear in the beam web can be manipulated by changing the length of the gusset-to-beam interface. In the case of the V or inverted-V condition, the vertical shear resulting from the moment is related to the horizontal shear at the

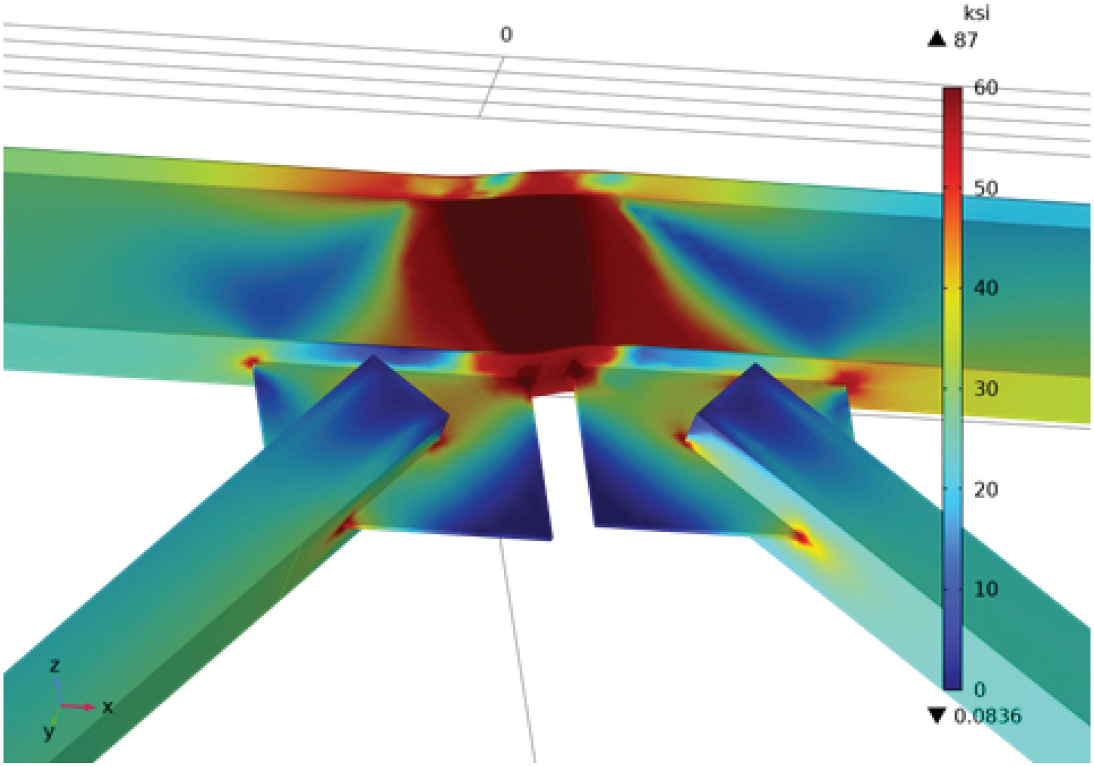

Fig. 6. Von Mises stress profile from FEA model of inverted-V connection with discontinuous gusset.

bottom flange since the only moment present results from the shear itself.

Both the uniform stress method (USM) presented by Fortney and Thornton (2015, 2017) and the concentrated stress method (CSM) presented by Sabelli et al. (2021) convert the applied moment into a force couple, where the magnitude of the forces in the couple is used to determine the vertical shear demand on the beam. In this fashion, the vertical shear is dependent on the assumptions made to convert the moment to a force couple. The conversion of a moment to a force couple is particularly convenient where dissimilar materials are used, where cross sections are not uniform, or to approximate inelastic behavior. This conversion is not necessary for the web of a wide-flange (WF) beam, recognizing through mechanics of materials that when the only moment applied to a rectangular element is due to the offset (eccentricity) of a shear applied in a given direction, the shear stress in that direction is equal to the shear stress in the orthogonal direction. Therefore, in an isotropic material such as steel, resolving the state of stress at the most critical section inherently resolves the state of shear stress in the orthogonal direction.

To illustrate, Figure 7(a) shows a profile of the lower half of the beam over the length of the gusset plate with the required forces assuming all vertical shear from the braces is distributed to the gusset plate. The forces on this section of the beam are identical to those assumed to act on a typical extended single plate as shown in Figure 7(b), except that the conditions are rotated 90° from one another. A similar diagram results when looking at the left half of a simply supported beam with a concentrated load at the center, which can also be a good illustration of how average horizontal and vertical shear stress are equal in an isotropic beam with uniform cross section. In the design of a bare steel beam, only vertical shear is evaluated, recognizing that horizontal shear is inherently addressed in doing so. Under the extended single-plate methodology in AISC *Manual* Part 10, only the critical stress state along a vertical plane is evaluated under the interaction of shear and moment, recognizing that the horizontal shear state is inherently addressed. The same can be done for the beam web in the V and inverted-V condition except that the critical stress state is along the horizontal plane at a distance of k from the bottom of the beam, where k is the design distance from the face of the beam flange to the intersection of the fillet with the web.

The interaction equation for extended single-plate connections in AISC *Manual* Part 10 (Equation 10-8) differs slightly from AISC *Manual* Equation 9-1 in that both the shear and moment ratios are squared and no axial ratio is included. Because a vertical normal force, such as from gravity loads, could be present in many instances, it is recommended that AISC *Manual* Equation 9-1 be used as it was for evaluation of the gusset plate. AISC *Specification* Section J10.2 allows for a distance of 2.5k to be added to each available side of the bearing length when evaluating the limit state of web local yielding. It is obvious this increase in length is available to resist horizontal shear as well. Therefore, it is reasonable to take advantage of this increased length when evaluating the forces on the beam web. Additionally, the moment at the critical section in the web (intersection with the fillet) could be reduced, recognizing that the eccentricity is decreased by the k dimension at the critical location. The authors generally recommend reserving use of the additional length of section and reduced moment for the evaluation of existing structures.

In continuation of the example, the available LRFD capacities of the beam web for the limit states of shear yielding and flexure, respectively, are determined as:

$$\begin{aligned}\phi R_{n-yield} &= \phi 0.6 F_y A_{gv} \qquad (10)\\ &= 1.0(0.6)(50\text{ ksi})(0.315\text{ in.})(50\text{ in.})\\ &= 473\text{ kips}\end{aligned}$$

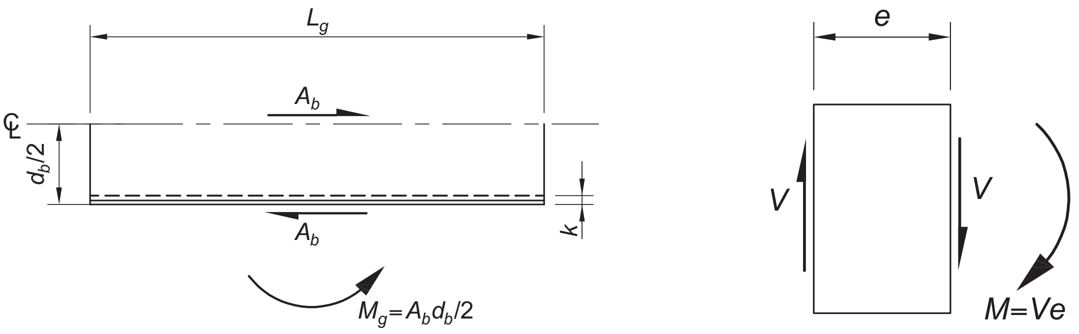

(a) Portion of beam between gusset and beam centerline

(b) Extended single plate

Fig. 7. Free-body diagram.

$$\phi M_{n-yield} = \phi F_y Z_g \tag{11}$$
$$= 0.9(50\text{ ksi})\frac{(0.315\text{ in.})(50\text{ in.})^2}{4}$$
$$= 8{,}859\text{ kip-in.}$$

Per AISC *Manual* Equation 9-1 the interaction for planar stresses on the beam web is determined as:

$$\frac{M_r}{M_c}+\left(\frac{P_r}{P_c}\right)^2+\left(\frac{V_r}{V_c}\right)^4 = \frac{3{,}580\text{ kip-in.}}{8{,}859\text{ kip-in.}}+\left(\frac{400\text{ kips}}{473\text{ kips}}\right)^4 \tag{12}$$
$$= 0.915 < 1.0 \quad \textbf{o.k.}$$

Web local crippling is the final check for local effects on the beam, for which the traditional approach of converting the required moment into a force couple is taken assuming a plastic stress distribution. The required demand is determined as:

$$R_u = \frac{M_u}{\frac{L_g}{2}} \tag{13}$$
$$= \frac{3{,}580\text{ kip-in.}}{\frac{50\text{ in.}}{2}}$$
$$= 143\text{ kips}$$

Using AISC *Manual* Equation 9-64a, the available strength is determined as:

$$\phi R_n = 2\left[\phi R_5 + l_b(\phi R_4)\right] \tag{14}$$
$$= 2\left[42\text{ kips} + (25\text{ in.})(3.60\text{ kips/in.})\right]$$
$$= 264\text{ kips} > 143\text{ kips} \quad \textbf{o.k.}$$

Lastly, the weld may be evaluated using AISC *Manual* Table 8-4 for the condition where k, as defined in the weld diagram, is taken equal to zero. Setting the eccentricity, $al = d_b/2$ results in $a = (17.9\text{ in.})/[2(50\text{ in.})] = 0.179$. Interpolation within the table results in the coefficient, $C = 3.58$. The required weld size in 16ths of an in., assuming $C_1 = 1.0$ for E70XX electrodes, is then determined as:

$$D \ge \frac{P_u}{\phi C C_1 L_g} \tag{15}$$
$$= \frac{400\text{ kips}}{0.75(3.58)(1.0)(50\text{ in.})}$$
$$= 2.98$$

Therefore, use a 3⁄16 in. fillet weld.

To ensure ductility and recognizing it as one of the fundamental requirements of the LBT, it is prudent to verify that the weld can develop the lesser strength of the gusset plate or the beam web. This can be done by recognizing that the condition of loading and detailing is generally consistent with that of extending single-plate connections such that the weld size need only meet or exceed ⅝t_p, where t_p is taken as the lesser of the gusset plate and beam web thicknesses. Under this approach, the required weld size to ensure ductility is determined as:

$$t_{weld} \ge 0.625 t_w \tag{16}$$
$$= 0.625(0.315\text{ in.})$$
$$= 0.197$$

Therefore, it is recommended to increase the fillet weld size by ¼ in.

The interaction on the beam calculated in the example was 0.915, suggesting the gusset plate was slightly longer than the minimum required. By iteration, the gusset length optimized to result in an interaction of 1.0 is found to be 48.5 in. It is often desirable to determine a required gusset length from the outset of design prior to checking other limit states. The shear term in AISC *Manual* Equation 9-1 can be conservatively squared rather than taken to the fourth power to conveniently allow for the gusset length to be isolated in the equation. Because this is a more conservative formulation, it is reasonable to take advantage of the $5k$ increase in effective web length mentioned previously. The result is a required gusset length determined as:

$$L_{g,\min} = \sqrt{\frac{4M_r}{\phi F_y t_w}+\left(\frac{P_r}{\phi F_y t_w}\right)^2+\left(\frac{V_r}{\phi 0.6 F_y t_w}\right)^2} - 5k \tag{17}$$

Using this equation for the previous example results in a required length of 48.3 in., nearly matching the length required by iteration using AISC *Manual* Equation 9-1.

The design is adequate by calculation under the applicable limit states. Figure 8 shows the stress profile of the example connection with the continuous gusset. Contrary to the discontinuous model shown in Figure 6, the continuous gusset model exhibits minimal local deformation and stresses well below yield in the upper portion of the beam web between braces. Comparison of the continuous gusset model to the discontinuous gusset model affirms a distribution of shear to both the gusset and beam web. The continuous model also illustrates aspects of the LBT—namely, that minimal inelastic strain (evident in the lower portion of the beam web) is needed to redistribute stress. The field of high stress is most prominent at the bottom of the beam web where moment is highest, then dissipates to lower levels near the center of the beam where shear is assumed to have been transferred to the workline and moment is assumed to be zero. This behavior is consistent with the idealized shear and moment model of Figure 7(a). For this reason, the connection can be assumed to behave essentially elastic from the perspective of global analysis of the frame, though some local yielding is likely to exist. The example using the continuous gusset supports the use of properly proportioned gusset plates to address the transfer of vertical shear using the LBT.

While inelastic deformations can be accommodated in many ways, it is generally desirable to provide ductility through global material yielding rather than highly localized yielding (stress concentrations) or buckling. As such, where WF beams are used in a web-vertical orientation, it is prudent to utilize beam sections that are not susceptible to shear buckling of the web—that is, beam sections should satisfy the h/t_w limit in AISC *Specification* Section G2.1(a) (AISC, 2022a). As noted in the example, proportioning welds to develop the lesser strength of the gusset plate or beam also ensures ductility.

TRUSS CONNECTIONS

Another application of this method is for truss web-to-chord connections. Trusses often utilize WF chord members with webs oriented vertically to improve flexural properties where loading occurs between truss panel points. Simple-span trusses can be highly optimized to save material such that relatively light chord members are used near the truss supports where chord axial forces are low. These same locations have the largest axial forces in the truss web members as these are the locations of the greatest global shear in the truss. By designing the gusset to transfer all vertical shear, such as along section A in Figure 9, the lighter chord members can be used without a need for doubler plates to address a potential shear overstress. The interface forces shown in Figure 9(b) reflect this redistribution of all shear to the gusset plate, which is the equivalent at setting $\Delta V_b = V$ in Figure 2. Conversely, toward the center of a simple-span truss where chord members tend to be heavy and axial forces in truss web members are low, shear can be distributed primarily to the chord member to potentially achieve more efficient gusset plates.

BRACE-TO-COLUMN CONNECTIONS

As illustrated by Sabelli et al. (2021), the force distribution at braced frame beam-to-column connections with a common gusset plate for both the brace and beam connections has similar force actions to V and inverted-V connections at brace intersections. Where the horizontal components of the brace forces, shown as H_1 and H_2 in Figure 10, are

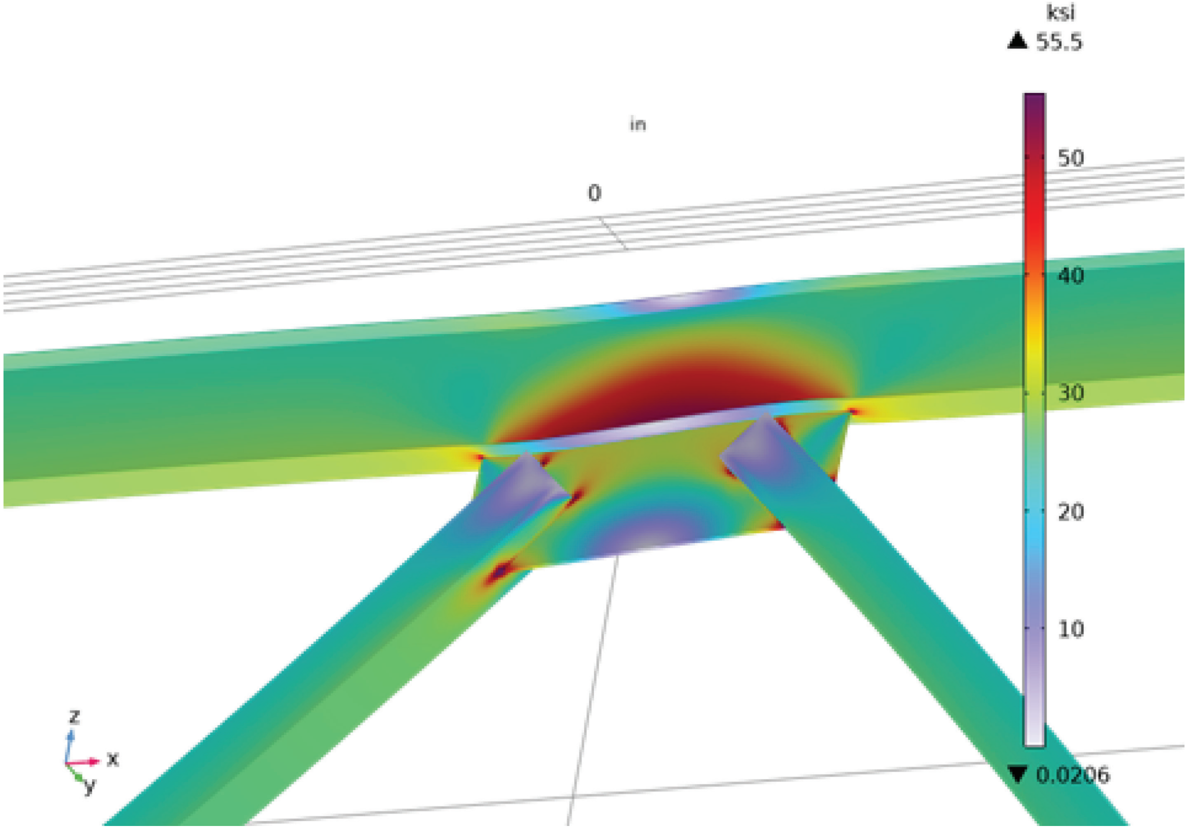

Fig. 8. Von Mises stress profile from FEA model of inverted-V connection with continuous gusset.

assumed to be transferred into the column, the column can often be deficient in shear capacity. The shear to the column can be reduced by redistributing some or all of the horizontal forces to the gusset plate. The gusset plate can then be proportioned to provide sufficient capacity to carry the required shear. The gusset-column interface designed for the moment must satisfy statics under the redistribution.

The moment resulting from the brace connection above the brace, the moment from the beam-to-column connection, if any, and the moment from the brace connection below the beam can be summed and addressed as a total moment, M_g, resolved over the full length of the interface, L_g, as shown in Figure 10. Note that the condition in Figure 10 assumes the bolt groups connecting the beam web to the gusset plate are designed for the eccentricity measured from the center of the respective bolt groups to the face of the column. In this manner, no moment from the beam-to-column connection is applied to the gusset-column interface. The column is assumed to be designed for the largest unbalanced moment, M_c, resulting from the beam connections on each side imposing their vertical end reactions, V_{b1} and V_{b2}, at their respective column faces. These assumptions are commonly made within commercial software for column design. Here the unbalanced moment is conservatively shown, assuming V_{b1} is at full force while V_{b2} is taken as zero.

As an alternate approach to the design of the gusset-column interface, the moments may be addressed independently over their respective compartmentalized connection lengths, L_1 and L_2, in the case of Figure 10(b). The former approach described in the previous paragraph is generally more economical as the section properties over the full length of the gusset plate are more effective as the square of the larger length rather than the sum of the squares of shorter lengths. On the other hand, the latter compartmentalized approach can be more effective in addressing many different brace configurations in design schedules, as the detailer may be able to select individual designs for each compartment from separate schedules. For example, the detailer could select parameters from design tables for the condition of a brace above a beam, parameters for a different condition of a brace below the beam, and parameters from perhaps a separate table that addresses the beam connection interface forces over the depth of the beam. All parameters from these conditions are then combined to detail the overall condition—in this case, of braces above and below a beam.

Similar to the beam condition, redistribution of shear from the column to the gusset plate may depend on inelastic behavior of the panel zone within the column. If such behavior is deemed undesirable, perhaps for reasons such as serviceability or resiliency, the panel zone could be strengthened by upsizing the column or adding doubler plates in an elastic design with relatively small building drifts. Alternatively, panel zone stresses could be reduced by increasing the length (vertical dimension) of the gusset. For extreme events such as seismic, some inelastic action in the columns is anticipated due to large story drifts. Strengthening the panel zone, or increasing the gusset length, to avoid shear yielding may simply force flexural yielding just above and/or below the connections to accommodate drifts.

Columns in seismic braced-frame systems must be moderately ductile or highly ductile in accordance with the AISC *Seismic Provisions* (AISC, 2022b) to accommodate such inelasticity. One approach to minimize column deformations due to building drifts is to rotate columns such that gusset plates are connected to the web of WF columns. The out-of-plane flexibility and relatively small out-of-plane flexural strength of the WF web can accommodate gusset rotation with minimal localized inelastic behavior as discussed in the AISC *Seismic Provisions* Commentary. Using the UFM, connections to the column web mathematically

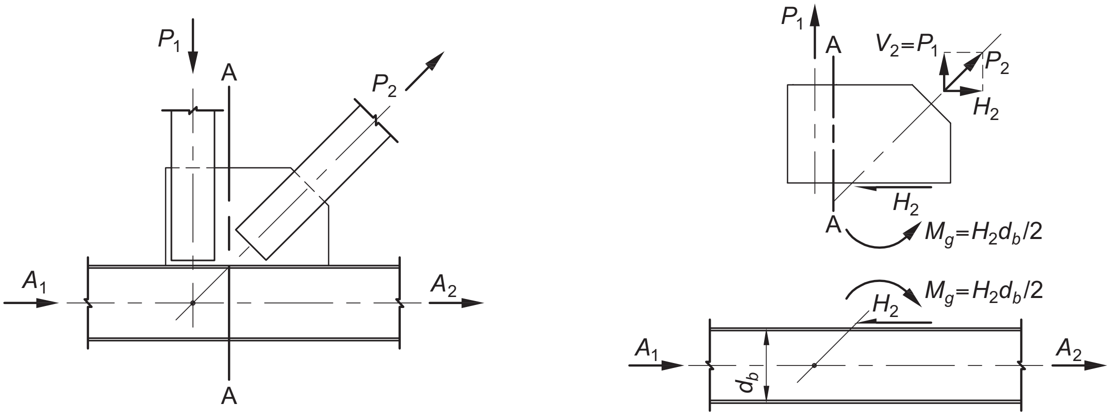

(a) Connection assembly *(b) FBD illustrating load transfer*

Fig. 9. Common truss connection.

eliminate shear in the column, thereby obviating the chevron effect. This is because the location of load application is effectively at the workline of the column such that any offset (eccentricity) over which vertical shear would need to be transferred is eliminated.

SUPER-X BRACE CONNECTIONS

Super-X brace configurations are often treated as a combination of a V configuration above a beam and an inverted-V configuration below the same beam. While free-body diagrams can be developed that illustrate similar gusset-to-beam connection force transfers in each of these configurations, it should be recognized that the global load paths differ. Where braced frames consist entirely of either V or inverted-V configurations at all levels, forces are transferred from the braces above a beam into the beam as an axial force, then transferred again to the braces below the beam at another location. In super-X configurations, forces from the braces above the beam are transferred through the beam to the braces below the beam at a singular location in a localized manner. Any axial forces in the beam are primarily collector forces only. Thus, the brace force transfer through the beam is dominated by axial behavior. Because the axial stresses from braces in one direction are compressive and tensile in the opposite direction, the combined stress state within the beam web can be transposed to a state of shear stress. This state is illustrated in Figure 11, where the braces above and below the beam are oriented at a 45° angle of inclination and assumed to be of equal magnitude, such as in a multi-tier braced frame. From this condition, it is evident that if the beam web is inadequate to transfer the axial forces from the braces, then the web is inherently inadequate for the transposed shear state. This helps to explain why the chevron effect appears to be an issue in super-X configurations more so than repeated V or inverted-V configurations as surmised by Sabelli and Saxey (2023).

The super-X connection can be addressed as a transfer of horizontal and vertical shears, with the vertical shears redistributed to the gusset plates above and below the beam just as in the V and inverted-V illustrations. This approach again depends on the inelastic behavior of the beam web to provide sufficient ductility for the redistribution of forces. As an illustration, assume a two-story multi-tier brace configuration, where the story shears above and below the beam are equal using the brace forces and member sizes from the example presented previously in an inverted-V configuration. By redistributing the entire vertical shear associated with each story to the respective gusset plates above and below the beam, the resulting shear state in the beam is due only to the moments at the top and bottom beam faces, which are additive. As discussed previously, methods that resolve these moments into force couples to

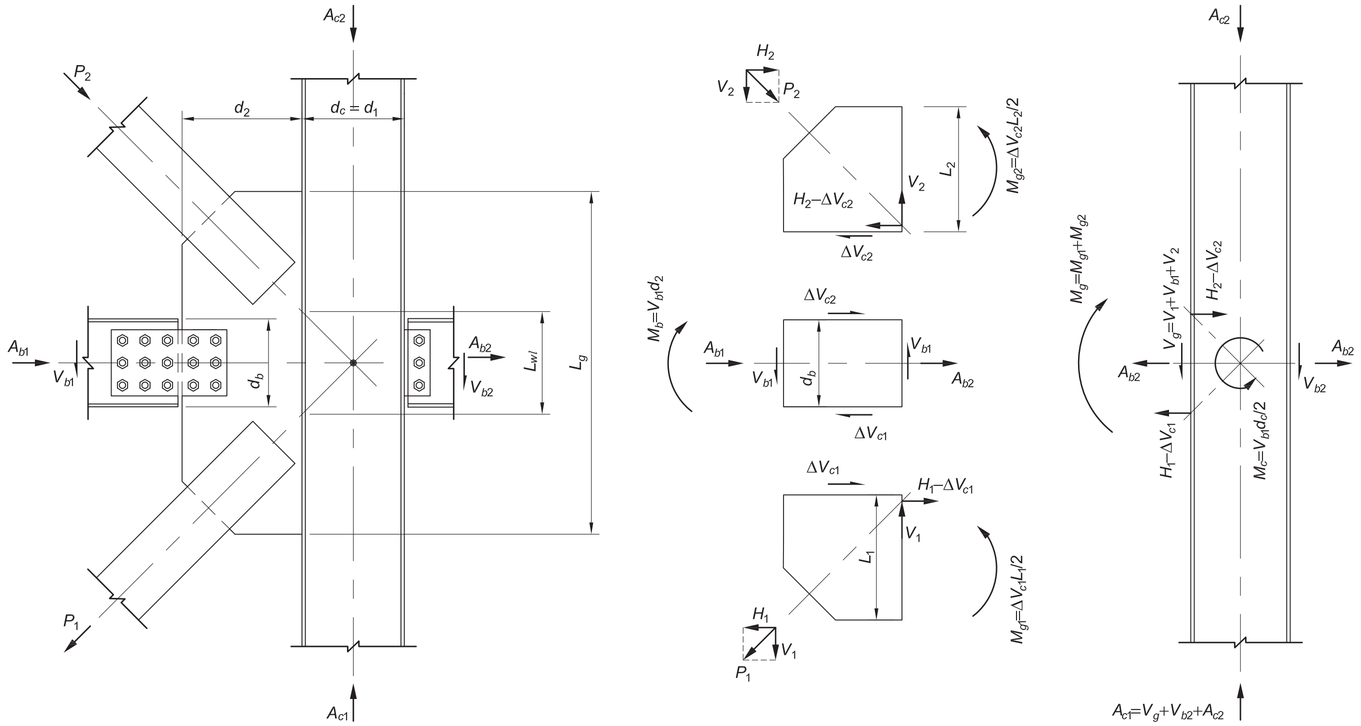

(a) Connection assembly

(b) FBD illustrating load transfer

Fig. 10. Brace connection to column.

obtain a required vertical shear are approximate by nature and can result in a state of stress that deviates somewhat from basic mechanics of materials to account for inelastic behavior.

AISC *Manual* Equation 13-33 is derived using the USM, assuming the full beam depth is used to resist shear imposed by a gusset at either face. As such, the moments above and below must be conservatively added to arrive at a total vertical shear to be resisted by the full beam depth. For the example shown previously, the gusset length, L_g, required by AISC *Manual* Equation 13-33a is 42.3 in. for a single-sided condition. For a super-X configuration where the loading above and below the beam are the same, such as in a multi-tier braced frame, the total additive moment is double that of the single-sided condition, resulting in a required gusset length of 84.6 in., which is greater than the 50 in. detailed in the example.

Recall that a single-sided gusset length of 48.5 in. was required using the interaction method from the example problem. This required length is greater than that determined using the USM because the USM considers normal forces and shear forces independently (no interaction). The diagrams shown in Figure 7 illustrate that addressing the moment and horizontal shear applied by the gusset on one face of the beam inherently resolves the shear over the half-depth of the beam adjacent to the gusset. Applying a gusset to both sides of the beam simply creates an additional state of stress in the web on the opposing side of the beam centerline. Figure 12 illustrates this through modeling of the super-X condition wherein the forces in the braces above the beam are of the same magnitude as the those below (the gusset conditions are effectively mirrored about the beam centerline). Examination of the stress contours in comparison to the one-sided condition of Figure 6 show that the state of stress above the beam centerline is essentially a mirror image of the condition below as expected. This illustrates that the super-X configuration is no more severe than the single-sided condition with regard to the magnitude of maximum shear stress. The state of stress is simply present on both sides of the beam centerline (through the full depth) in the super-X configuration. Thus, gusset and beam design can be compartmentalized such that addressing each gusset condition independently, using the interaction method shown in the example, ensures an acceptable maximum state of stress within the beam web. Further, the required gusset length for each gusset remains 48.5 in. as opposed to the significantly more conservative 84.6 in. using the USM.

The CSM developed by Sabelli et al. (2021) derives a vertical shear resulting from an approximate force couple model that is more accurate than that of the USM. For example, a required length approximated using Equation 5 from Sabelli and Bolin (2022) using the nomenclature herein is determined as:

$$\begin{aligned} L_g &= \frac{1.25 M_{tot}}{\phi V_n} \qquad (18) \\ &= \frac{1.25(400\text{ kips})(17.9\text{ in.})}{169\text{ kips}} \\ &= 53.0\text{ in.} > 50\text{ in.} \quad \textbf{n.g.} \end{aligned}$$

This value is substantially less than that calculated using the USM but still exceeds the 50 in. detailed. Sabelli et al. (2021) provide for progressively more rigorous calculations to refine the required length if needed. Considering Equation 39 from Sabelli and Saxey (2021) recognizing the moments above and below the beam are each half of the total moment, the required length is determined as:

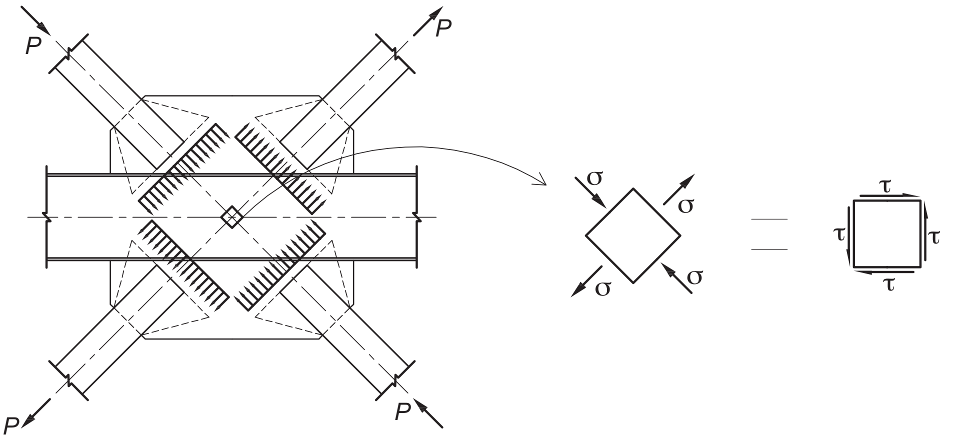

(a) Distribution from gusset plate

(b) Approximate normal stress state in the web

(c) Rotation creates pure shear stress

Fig. 11. Axial stress distribution in super-X connection.

$$L_g = \frac{M_g}{0.5\phi V_n} + \frac{0.5\phi V_n}{\phi F_y t_g} \tag{19}$$

$$= \frac{3{,}580 \text{ kip-in.}}{84.5 \text{ kips}} + \frac{84.5 \text{ kips}}{0.9(50 \text{ ksi})(0.5 \text{ in.})}$$

$$= 46.1 \text{ in.} < 50 \text{ in.} \quad \textbf{o.k.}$$

This value is slightly less than the 48.5 in. determined using the interaction approach. Sabelli et al. (2021) provide for further refinements that could reduce the required length slightly below 46.1 in. These methods also consider the limit states under normal forces independently of those under shear forces rather than addressing in a combined interaction, which explains the modestly lower length as compared to the interaction method.

As an alternative to the UFM using the USM, CSM, or interaction approach, the axial force transfer can be addressed directly by simply carrying the forces on the Whitmore sections (AISC *Manual* Part 9) for each brace into the web of the beam and designing for those forces directly. In this manner, several approaches can be taken to address a deficiency in beam-web capacity. For example, the length of the brace-to-gusset connection could be increased, thereby increasing the width of the Whitmore section and reducing the stress on the beam web. This approach increases gusset size, which is an analogous solution to determining an adequate gusset length using the USM or CSM. Note that overlap of the Whitmore sections for opposing braces is acceptable, recognizing that the opposing stresses do not occur in the same direction and are, thus, not additive. The effect of these increases in connection length, gusset size, and Whitmore section width to reduce stress is illustrated in Figure 13. Regarding local web stability using this method, the vertical force component on the projected Whitmore section should be checked in accordance with AISC *Specification* Section J10. Another method of addressing local web stability and a potentially deficient web is to provide diagonal stiffeners such as those shown in Figure 13. Of little surprise, these stiffeners effectively reinforce the panel zone for increased shear resistance. Downsides to this approach include more complicated welding at the interface of the skewed stiffener with the inside of the beam flange and potential complications with stiffener geometry, where braces above and below the beam occur at substantially different inclination angles. FEA has shown that adding vertical and/or diagonal stiffeners does change the locations of the highest stress within the beam web somewhat, but the overall behavior is unchanged.

This approach of axial force transfer using the Whitmore section can be applied to the super-X connection example considered previously. The connection parameters are shown in Figure 14, where the length of the brace-to-gusset connection is 12 in.

The length of the Whitmore section, l_{wh}, is determined by geometry as:

$$l_{wh} = (8 \text{ in.}) + 2(12 \text{ in.})\tan(30°) \tag{20}$$

$$= 21.9 \text{ in.}$$

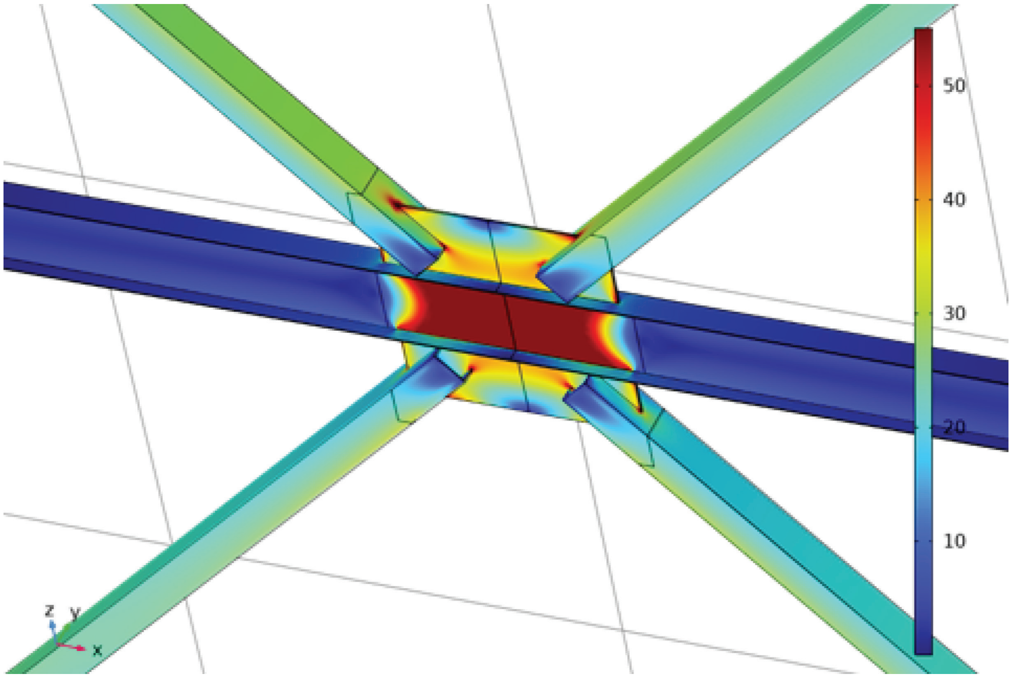

Fig. 12. Von Mises stress profile from FEA model of X connection.

The strength of the web for the limit state of axial yielding is determined as:

$$
\begin{aligned}
\phi P_n &= \phi F_y t_w l_{wh} && (21)\\
&= 0.9(50\text{ ksi})(0.315\text{ in.})(21.9\text{ in.})\\
&= 310\text{ kips} > 283\text{ kips} \quad \textbf{o.k.}
\end{aligned}
$$

This calculation assumes web buckling and web crippling limit states are checked separately or mitigated with stiffeners. At a demand/capacity ratio of 0.91 for the limit state of axial yielding, the web geometry is relatively well optimized, though there is room for further refined. Figure 14 shows that the required gusset length to develop the full Whitmore section into the beam is 43 in. This is close to the 46 in. determined using the CSM, particularly recognizing even more precise approaches can be taken to the CSM than illustrated herein. The 43 in. length is very close to 42.3 in. for a one-sided connection using the USM. While there is conjecture in the absence of a refined FEA model using a 42.3 in. gusset length, this suggests the USM as intended for one-sided connections is also appropriate for each side of super-X conditions. This does make sense as the final form of the equation relates to horizontal shear only. Accepting this equation as accurate but recognizing the top and bottom conditions are resolved on their respective halves of the beam, as discussed using the interaction approach, produces the most optimized length of the methods considered.

One advantage of the axial force approach using the Whitmore section is that the Whitmore length must be determined in evaluating the brace-to-gusset connection such that the check of this projected stress field on the member web is an intuitive additional step requiring little design effort. Another advantage is the correlation of the stress field on the beam web to the geometry of the brace-to-gusset connection. This correlation can serve to mitigate ill-proportioned gusset plates, where the length of the gusset may be increased without considering the brace-to-gusset connection. In extreme cases, such increases in gusset length could induce bending in the gusset plate that may not be accounted for by the designer. The implications of the axial force approach using the Whitmore section are somewhat profound in that gusset plates need only be proportioned to develop sufficient Whitmore length for each brace into the member web to inherently satisfy the shear state within the member. Note that where additional

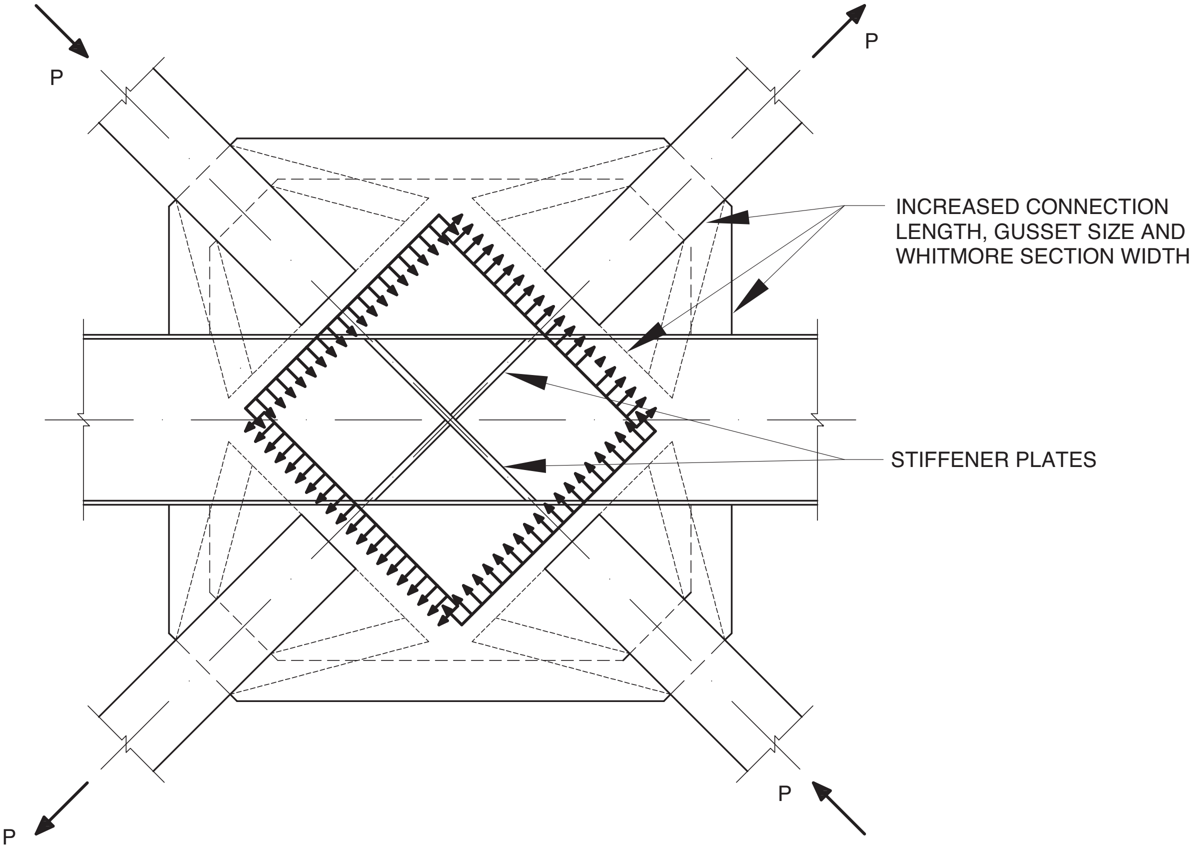

Fig. 13. Illustration of methods to address axial forces through beams in super-X connections.

axial forces are present, such as those from the beam at a beam-to-column condition, components of stress from overlapping stress fields contributing in the same direction would need to be combined to evaluate the total stress state at a given location.

SPECIAL CONSIDERATIONS FOR HSS MEMBERS

It is common in many structures to use a rectangular HSS strut as the horizontal member in a braced frame rather than a WF beam. Carrying forces through rectangular HSS members requires additional consideration. With the gusset plate centered on the horizontal face of the HSS member, the vertical walls of the HSS member (web members) are offset from the gusset plate rather than aligned. The horizontal face connected to the gusset plate typically lacks sufficient flexural strength to transfer appreciable vertical forces from the gusset plate to the HSS webs (side walls). Therefore, the gusset plate must be relied upon to transfer the entirety of the vertical components of force between braces through shear.

As discussed previously and shown in Figure 4, redistribution of vertical shear to the gusset plate results in a moment at the gusset-to-strut interface to resolve statics. Often the HSS is inadequate to transfer the vertical force couple associated with this moment due to insufficient wall plastification capacity. Figure 15 shows an FEA model of the same configuration and forces previously illustrated in Figure 12, except that the W18×40 has been replaced by a rectangular HSS18×6×⅜. The horizontal walls at the top and bottom of the HSS are inadequate to handle the moment imposed at the gusset-to-HSS interface, thereby violating a requirement of the LBT. Significant yielding with high strains and large associated gusset rotations resulted in the walls of the HSS flexing uncontrollably.

Several approaches can be taken to provide an adequate connection. One option is to increase the thickness of the HSS walls and/or the length of the gusset plate until the required forces can be resisted (increase the wall plastification capacity). Under large forces, upsizing these elements sufficiently may prove impractical. A second option is to relocate the workpoints of the braces to the faces of the HSS

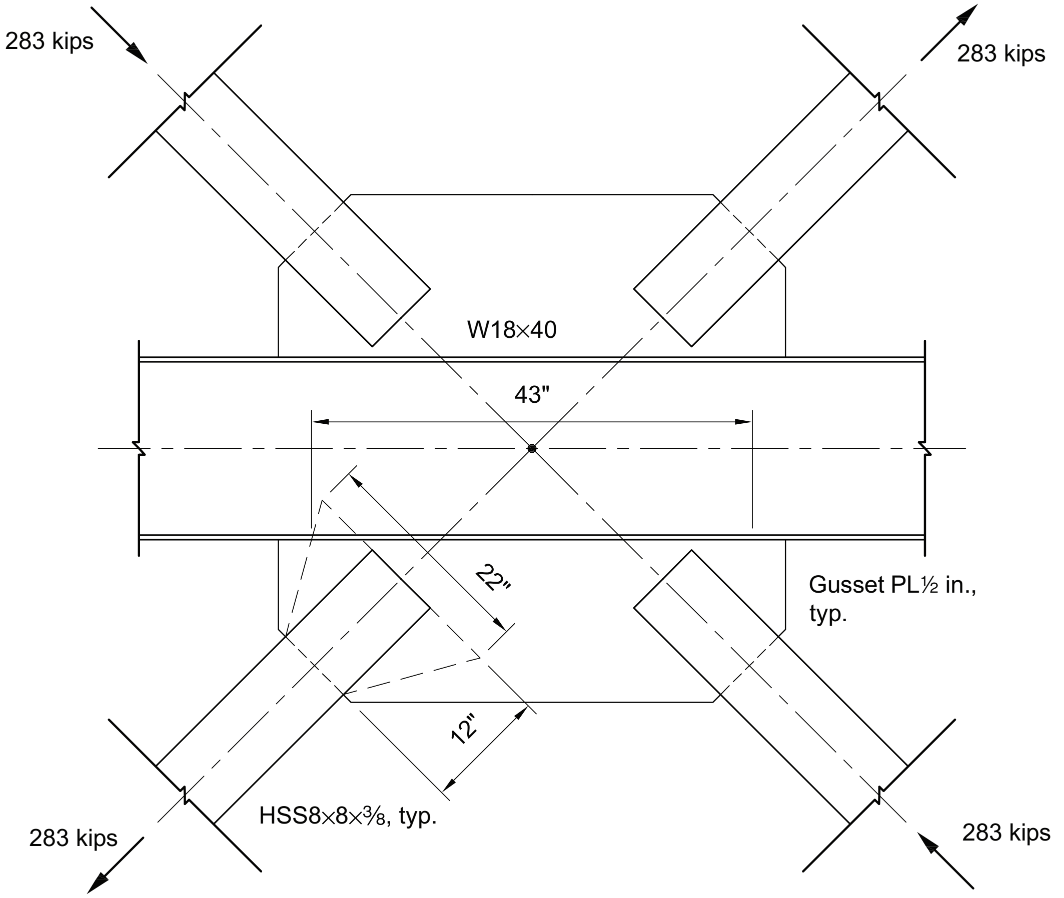

Fig. 14. Example super-X connection using Whitmore section axial force projection on beam web.

as shown in Figure 16(a). This approach requires only horizontal shear to be transferred at the gusset-to-HSS interface thereby eliminating the out-of-plane demands on the HSS wall. However, relocation of the workpoint imposes a flexure on the HSS member, which is resolved by vertical reactions at the member ends. The member must be designed for these actions, and any analysis should reflect the relocation of the workpoint by using rigid links or offsets. A third option is to slot the HSS and continue the gusset plate through both walls. This allows the required moment at the gusset-to-HSS interface to be addressed as a horizontal force couple through the longitudinal attachments to the HSS walls top and bottom, thereby eliminating the need for vertical force transfer transverse to the HSS walls. This approach is illustrated in Figure 16(b).

CONCLUSION

In conclusion, the chevron effect can have a significant impact on primary members depending on the approach taken to address the transfer of forces. The following conclusions are drawn from the discussions herein:

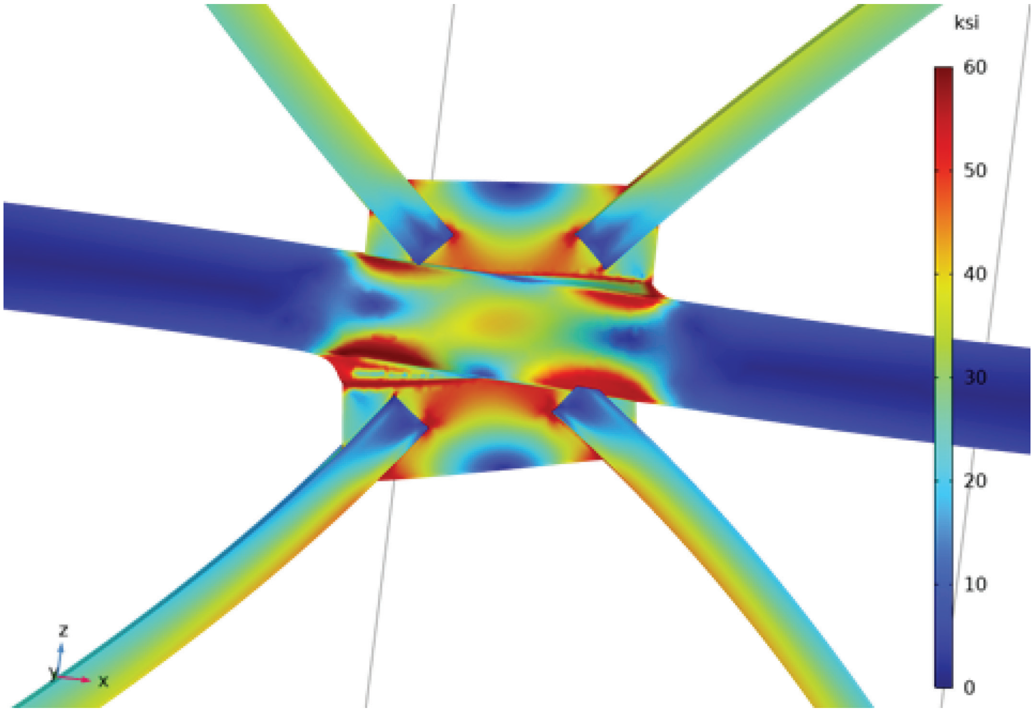

Fig. 15. Von Mises stress profile from FEA model of X connection with HSS horizontal strut.

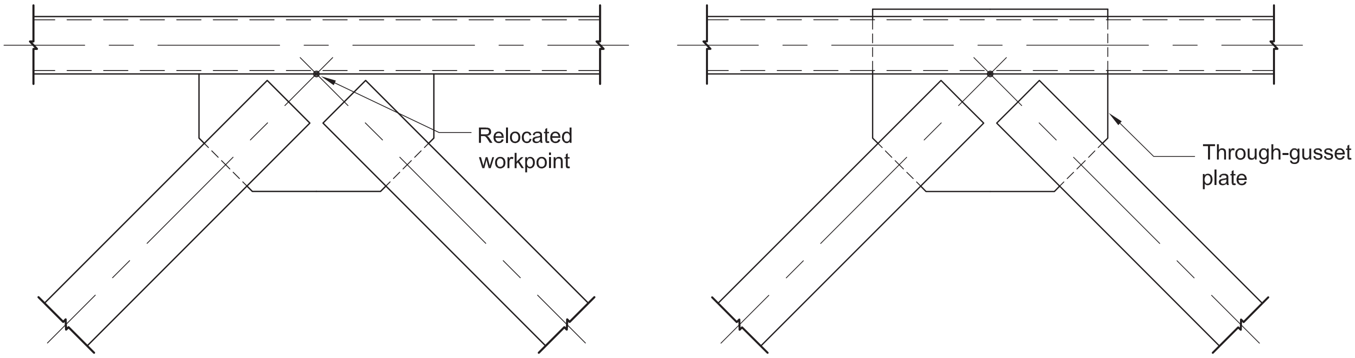

(a) Workpoint relocated to face of HSS

(b) Through-gusset plate at slotted HSS

Fig. 16. Inverted-V brace connections to HSS horizontal strut.

1. Redistribution of forces under the LBT, including proper proportioning of gusset plates, can reduce the required shear on beam or strut members in V, inverted-V, and super-X brace configurations.
2. Similarly, force redistribution can be used to manipulate the required shear on columns in brace and beam connections to columns using a common gusset plate or in truss chords at truss diagonal-to-chord connections.
3. Because of the reliance on ductile behavior to redistribute forces to an assumed load path, WF beams or columns in braced frames and truss chords are recommended to satisfy the h/t_w limit of AISC *Specification* Section G2.1(a).
4. Connecting beam and brace connections to the web of WF column members can reduce the shear demands on columns and inelastic strains resulting from large story drifts in extreme events, such as an earthquake.
5. In super-X configurations, the beam web can be evaluated, assuming an axial force transfer on the Whitmore sections for each brace. Gusset plates can be proportioned and/or stiffener plates utilized to avoid the addition of doubler plates or upsizing of primary members, which may enhance the overall economy.
6. The transfer of forces from gusset plates to HSS beam and column members may warrant the use of through-gusset plates or relocated workpoints to address insufficient out-of-plane capacity of the HSS walls.

REFERENCES

AISC (2022a), *Specification for Structural Steel Buildings,* ANSI/AISC 360-22, American Institute of Steel Construction, Chicago, Ill.

AISC (2022b), *Seismic Provisions for Structural Steel Buildings,* ANSI/AISC 341-22, American Institute of Steel Construction, Chicago, Ill.

AISC (2023), *Steel Construction Manual,* 16th Ed., American Institute of Steel Construction, Chicago, Ill.

ASTM (2021), *Standard Specification for High-Strength Low-Alloy Columbium-Vanadium Structural Steel*, ASTM A572/A572M-21e1, ASTM International, West Conshohocken, Pa.

ASTM (2023), *Standard Specification for Cold-Formed Welded and Seamless Carbon Steel Structural Tubing in Rounds and Shapes*, ASTM A500/A500M-23, ASTM International, West Conshohocken, Pa.

Barker, R.M. and Puckett, J.A. (2021), *Design of Highway Bridges—Based on AASHTO LRFD Bridge Design Specification*, 4th Ed., John Wiley and Sons, New York, N.Y.

Bower, A.F. (2010), *Applied Mechanics of Solids,* 1st Ed., CRC Press, Clermont, Fla.

Comsol Multiphysics (2023), Comsol Multiphysics®, v. 6.2, COMSOL AB, Stockholm, Sweden. www.comsol.com.

Fortney, P. and Thornton, W. (2015), “The Chevron Effect—Not an Isolated Problem,” *Engineering Journal*, AISC, Vol. 52, No. 2, pp. 125–168.

Fortney, P. and Thornton, W. (2017), “The Chevron Effect and Analysis of Chevron Beams—A Paradigm Shift,” *Engineering Journal*, AISC, Vol. 54, No. 4, pp. 263–296.

Muir, L. and Thornton, W. (2014), *Vertical Bracing Connections—Analysis and Design,* Design Guide 29, American Institute of Steel Construction, Chicago, Ill.

Sabelli, R. and Bolin, E. (2022), “The Chevron Effect: Reserve Strength of Existing Chevron Frames,” *Engineering Journal*, AISC, Vol. 59, No. 3, pp. 209–224.

Sabelli, R. and Saxey, B. (2021), “Design for Local Member Shear at Brace and Diagonal-Member Connections: Full-Height and Chevron Gussets,” *Engineering Journal*, AISC, Vol. 58, No. 1, pp. 45–78.

Sabelli, R. and Saxey, B. (2023), “Closure: Design for Local Member Shear at Brace and Diagonal-Member Connections: Full-Height and Chevron Gussets,” *Engineering Journal*, AISC, Vol. 60, No. 3, pp. 123–128.

Sabelli, R., Saxey, B., Li, C-H., and Thornton, W.A. (2021), “Design for Local Member Shear at Brace Connections: An Adaptation of the Uniform Force Method,” *Engineering Journal*, AISC, Vol. 58, No. 4, pp. 223–266.

Embedment Length of Steel Coupling Beams—Evaluation and Proposed Revision to the AISC *Seismic Provisions* for Ordinary Composite Coupled Walls

SUSHIL KUNWAR and BAHRAM M. SHAHROOZ

ABSTRACT

One of the composite systems codified in AISC 341 (2022) is composite coupled walls, which are comprised of two or more reinforced concrete structural (shear) walls linked by steel or composite coupling beams embedded in the wall piers. The embedment length is a critical factor that affects the stiffness and strength of the coupling beams—two factors that affect the overall performance of coupled walls. Past studies have examined the performance of special coupled walls in which the wall piers are heavily reinforced and typically have boundary elements. A recent series of tests focused on ordinary composite coupled walls demonstrated that the embedment length determined according to the 2022 edition of AISC 341 was insufficient to develop the target member strength. The results prompted a need to reevaluate the equation by which the embedment length is determined. Using basic principles supported by experimental data, a revised equation was developed and evaluated through numerical simulations. The revised equation results in longer embedment lengths by as much as nearly 40% for cases that would likely be encountered in practice.

Keywords: composite construction, coupling beam, coupled walls, embedment length, structural wall, shear wall.

INTRODUCTION

Coupled structural (shear) walls (CSW) are a common structural system. This system is comprised of two or more structural walls that are typically linked at each floor by coupling beams. Based on the expected level of inelastic deformations, composite structural (shear) walls can be classified as composite ordinary shear walls (C-OSW) or composite special shear walls (C-SSW). One common composite system involves linking reinforced concrete wall piers by steel (or steel-concrete composite) coupling beams that are embedded in the wall piers.

The required embedment length of the coupling beam, L_e, is calculated using Equation H4-4 from AISC 341 (AISC, 2022), hereafter referred to as AISC 341-22, shown here as Equation 1:

$$V_{n,connection} = 1.54\sqrt{f_c'}\left(\frac{b_w}{b_f}\right)^{0.66}\beta_1 b_f L_e\left(\frac{0.58-0.22\beta_1}{0.88+\frac{g}{2L_e}}\right) \quad (1)$$

where

L_e = embedment length of coupling beam measured from the face of the wall, in.

$V_{n,\,connection}$ = design shear strength, kips

b_f = width of beam flange, in.

b_w = thickness of wall, in.

f_c' = specified compressive strength of concrete, ksi

g = clear span of coupling beam, in.

β_1 = factor relating depth of equivalent rectangular compressive stress block to neutral axis depth, as defined by ACI 318-19 (2019)

This equation was developed by Mattock and Gaffar (1982) based on the data from monotonic testing of steel members (acting as brackets) embedded in precast columns. Prior to this study, Marcakis and Mitchell (1980) investigated the performance of precast concrete connections with embedded steel members subjected to monotonic loading. In addition to W-shapes, the embedded steel members in both studies included solid sections or HSS (filled or unfilled).

Including Mattock's and Marcakis's original tests, a database containing the data and results from 52 tests was

---

Sushil Kunwar, Research and Development Structural Engineer, Browder + LeGuizamon and Associates, Atlanta, Ga. Email: sushil@blaengineers.com (Former Doctoral Research Assistant, Department of CAECM, University of Cincinnati)

Bahram M. Shahrooz, Professor Emeritus, Department of CAECM, University of Cincinnati, Cincinnati, Ohio. Email: bahram.shahrooz@uc.edu (corresponding)

Paper No. 2024-05R

Table 1. Summary of Key Aspects of Available Research Data

Source	Number of Specimens	Loading	f'_c (ksi)	$\frac{g}{2d}$	$\frac{L_e}{d}$	Controlling Limit State
Marcakis and Mitchell (1980)*+	18	Monotonic	3.40–5.80	1.8–2.0	1.00-1.50	Connection strength
Mattock and Gaffar (1982)+	5	Monotonic	2.95–4.10	1.0–2.7	1.33-2.25	Connection strength
Shahrooz et al. (1993)*	3	Cyclic	4.82–5.62	2.2–2.3	1.89	Coupling beam M_p
Harries (1995)	4	Cyclic	3.75–6.25	1.3–3.5	1.43-1.73	Coupling beam M_p or V_p
Fortney (2005)*	3	Cyclic	5.13–5.30	2.6	2.18	Coupling beam V_p
Park et al. (2005) and Park and Yun (2006)*	9	Cyclic	4.35–4.93	0.9–3.4	1.07	Connection strength
Shahrooz et al. (2018)*	2	Cyclic	6.51	3.3	2.00	Coupling beam V_p
Kunwar and Shahrooz (2023)*	8	Cyclic	4.13–6.98	4.3–5.7	0.96-1.98	Connection strength

* Some or all specimens had auxiliary transfer bars.

+ Coupling beams in some specimens were solid sections or HSS (filled or unfilled)

d = Coupling beam depth

M_p = Plastic moment strength of the coupling beam

V_p = Plastic shear strength of the coupling beam

compiled, as provided in Table 1. Shahrooz et al. (1993) and Harries (1995) verified the applicability of Mattock-Gaffar's and Marcakis-Mitchell's equations for steel coupling beams subjected to cyclic loading. The controlling limit state in both studies was, however, either the plastic moment strength, M_p, or the plastic shear strength, V_p, of the steel coupling beam. Hence, the studies did not specifically evaluate the ultimate strength of the embedded connection. In several subsequent research programs, the connection strength had been enhanced by utilizing auxiliary transfer bars (reinforcing bars connected to the flanges to improve the bearing strength). Most of the past studies were focused on C-SSW in which the wall piers would be heavily reinforced and typically have boundary elements. A recent series of tests conducted by Kunwar and Shahrooz (2023) was focused on C-OSW with the connection strength being the controlling limit state. These tests demonstrated that the embedment length calculated by AISC 341-22, Equation H4-4 (Equation 1), was insufficient to develop the target member strength. To remedy the observed deficiency of Equation H4-4, a revised equation was developed by using basic principles in conjunction with relevant experimental data from the database, shown in Table 1. Derivation of the revised equation and its verification through test data and numerical simulations are presented in this paper.

DERIVATION OF A REVISED EQUATION

The database shown in Table 1 was filtered down to 10 specimens by focusing on (1) the tests with W-shapes that did not have auxiliary transfer bars, (2) those for which the connection strength was the controlling limit state, and (3) those with wall reinforcement similar to what would be placed in ordinary walls. The details of the 10 specimens are summarized in Table 2. Using the data from this table and the model shown in Figure 1, a revised equation for calculating embedment length was developed.

The bearing stress between the steel coupling beam flanges and the surrounding concrete was modeled according to Hognestad's (1951) concrete constitutive relationship that has a parabolic ascending branch and a linear post-peak descending branch. The peak concrete strength, f_c, was taken as $0.85\psi f'_c$ with ε_{01} and ε_{085} set equal to 0.002 and 0.0038, respectively. The selected value of 0.85 in the present derivation is intended to approximately account for nonuniformity of concrete compressive strength over the wall height. The bearing forces, C_f and C_b, were obtained by integrating the bearing stress distributed over the embedment length, L_e, and the coupling beam flange width, which was increased by a factor labeled α. This factor is intended to account for spreading of bearing stresses. Note that bearing stress is integrated over the depth of the neutral axis, c, to determine C_f and over $(L_e - c)$ for C_b.

The magnitude of applied shear, V, was incrementally increased, and the values of the strain at the wall-coupling beam interface, ε_f, and the depth of the neutral axis, c, were iterated until equilibrium of the vertical forces and moment could be achieved. The connection strength was taken as the maximum V for which equilibrium was possible. Figure 1(a) illustrates the case with $\varepsilon_f > \varepsilon_{01}$ and $\varepsilon_b < \varepsilon_{01}$; however, these strains were changed as needed in the iteration process.

During iteration, several options were considered to define the peak concrete strength (i.e., the value of coefficient ψ)

Table 2. Details of Specimens Used for Model Development

Source	Specimen ID	Specimen Scale	b_w (in.)	b_f (in.)	d (in.)	g (in.)	L_e (in.)	L_e/d	Critical Mode	f'_c (ksi)	V_{test} (kips)
Mattock and Gaffar (1982)	W4	N/A	10.0	4.00	6.00	12.0	8.00	1.3	Shear	2.95	24.1
Kunwar and Shahrooz (2023)	SK-1	½	10.0	4.03	6.28	36.0	6.00	0.96	Flexure	4.13	14.2
	SK-2	½	10.0	4.03	6.28	36.0	7.00	1.1	Flexure	4.13	20.4
	SK-3	½	10.0	5.27	8.28	36.0	13.0	1.6	Flexure	6.95	49.0
	SK-4	½	10.0	5.27	8.28	36.0	13.0	1.6	Flexure	6.95	47.4
	SK-5	¾	15.0	8.05	12.1	54.0	19.0	1.6	Shear	6.98	109
	SK-6	¾	15.0	8.05	12.1	54.0	24.0	2.0	Shear	4.70	113
	SK-8	¾	15.0	8.05	12.1	54.0	19.0	1.6	Shear	6.15	89.7
Park et al. (2005) and Park and Yun (2006)	SCB-ST	⅓[a]	11.8	6.89	13.8	47.2	14.7	1.1	Flexure	4.93	70.4
	HCWS-ST	⅓[a]	11.8	6.89	13.8	47.2	14.7	1.1	Flexure	4.35	60.3

N/A: Could not be inferred due to inconsistencies between the cover to reinforcement and the other dimensions/bar sizes.
[a] Inferred based on the dimensions and bar sizes.

and the amount of spreading of bearing stresses (i.e., factor α). Finally, the most reasonably close match of the measured connection strength (V_{test} in Table 2) was found to be achieved by setting ψ equal to β_1 and taking α as the lesser of 1.3 and b_w/b_f, where b_w is wall pier thickness and b_f is coupling beam flange width.

The measured connection strengths are compared against those obtained from the final iteration (with $\psi = \beta_1$ and α = lesser of 1.3 and b_w/b_f) in Figure 2. The largest differences are for four cases (specimens SK-1, SK-2, SCB-ST, and HCWS-ST) with $L_e/d \leq 1.1$, where d is the depth of the coupling beam. For such cases, the embedment

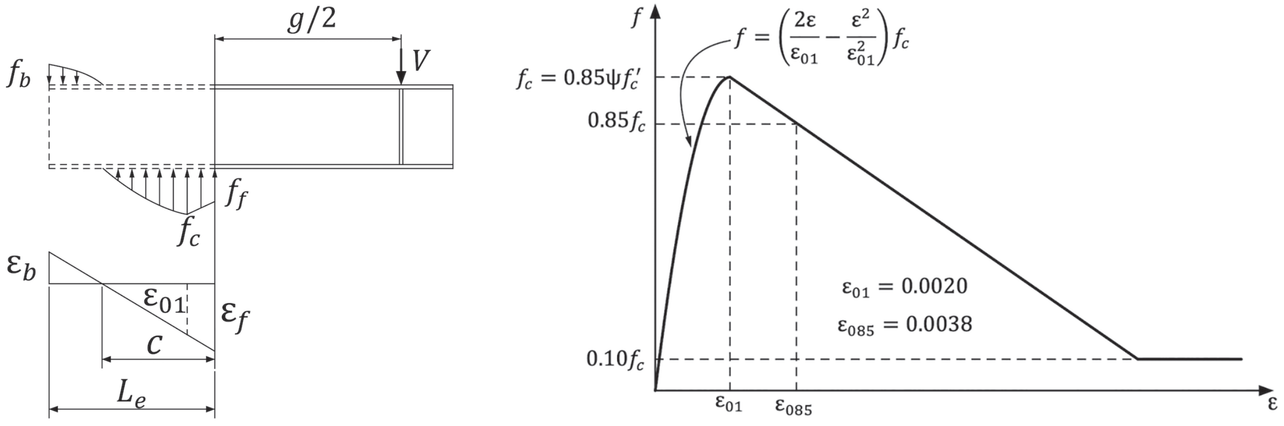

(a) Stress distribution

(b) Concrete model

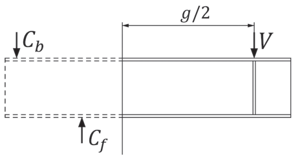

(c) Bearing forces

Fig. 1. Assumed stress distribution and concrete model for development of revised equation.

Table 3. Values of ε_f and c/L_e after Iteration

Source	Specimen ID	ε_f	c/L_e
Mattock and Gaffar (1982)	W4	0.0040	0.60
Kunwar and Shahrooz (2023)	SK-3	0.0038	0.57
	SK-4	0.0038	0.57
	SK-5	0.0037	0.56
	SK-6	0.0037	0.57
	SK-7	0.0036	0.56

region is characterized as a "D region," where the strain variation along the embedment length is more complex than the linear distribution shown in Figure 1(a), and the use of a strut-tie method is more appropriate (Kunwar and Shahrooz, 2023). Ignoring the cases with $L_e/d \leq 1.1$, the measured connection strength is on average 1.17 times larger than the shear strength obtained from iteration with a coefficient of variation of 0.18.

Table 3 summarizes the values of ε_f and c/L_e (depth of the neutral axis normalized with respect to embedment length) corresponding to the values of V obtained from the final iteration, which are shown on the y-axis in Figure 2. As discussed previously, the strain is not distributed linearly along the embedment length for cases with L_e/d close to 1. Therefore, the results in Table 3 are provided only for the cases with $L_e/d > 1.1$. The average values of c/L_e and ε_f are 0.57 and 0.0038, respectively, with the corresponding coefficient of variation equal to 0.043 and 0.023. Setting $c/L_e = 0.57$ and $\varepsilon_f = 0.0038$ in the model depicted in Figure 1, Equation 2 was derived. Note that V_n, the nominal shear strength, in Equation 2 is the same as V shown in Figure 1 and used in the previous discussions. In this equation, α accounts for spreading of bearing stresses against the flanges.

$$V_n = \frac{0.19\alpha\beta_1 f_c' b_f L_e}{0.57 + \dfrac{g}{2L_e}} \quad \text{where } \alpha = \frac{b_w}{b_f} \leq 1.3 \tag{2}$$

It should be noted that AISC 341-22, Equation H4-4 (Equation 1), was derived based on the average value of $c/L_e = 0.66$ and $\varepsilon_f = 0.003$ and bearing stress $= 1.54\sqrt{f_c'}$. According to ACI 318-19, bearing stress is directly proportional to f_c' (and not $\sqrt{f_c'}$), which is consistent with the approach followed for the derivation of Equation 2. Spreading of bearing stresses in the current equation is represented by $(b_w/b_f)^{0.66}$.

EVALUATION OF REVISED EQUATION

The revised equation was evaluated by comparing the shear strengths calculated from Equation 2 versus the test results shown in Table 2. Additional comparisons were made

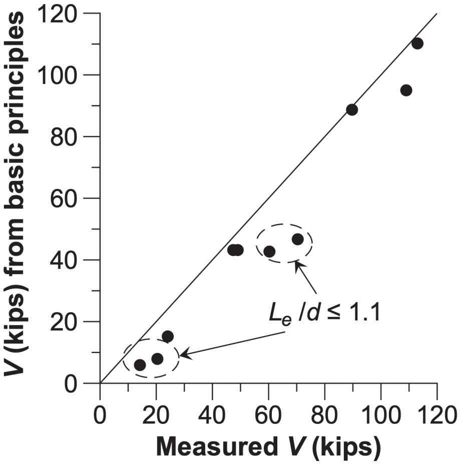

Fig. 2. Comparison of measured strengths and connection strengths from basic principles.

Table 4. Calculated Nominal Shear Strengths vs. Measured Values

Source	Specimen ID	L_e/d	Critical Mode	V_{test} (kips)	$V_{n,\ calculated}$ (kips)		$V_{test}/V_{n,\ calculated}$	
					Current Equation	Revised Equation	Current Equation	Revised Equation
Mattock and Gaffar (1982)	W4	1.3	Shear	24.1	31.8	15.0	0.76	1.61
Kunwar and Shahrooz (2023)	SK-1	0.96	Flexure	14.2	11.8	5.8	1.20	2.44
	SK-2	1.1	Flexure	20.4	15.5	7.7	1.32	2.65
	SK-3	1.6	Flexure	49.0	55.9	42.1	0.88	1.16
	SK-4	1.6	Flexure	47.4	55.9	42.1	0.85	1.12
	SK-5	1.6	Shear	109	122	92.7	0.90	1.18
	SK-6	2.0	Shear	113	159	109	0.71	1.04
	SK-7	1.6	Shear	89.7	118	86.4	0.76	1.04
Park et al. (2005)	SCB-ST	1.1	Flexure	70.4	64.4	45.5	1.09	1.55
	HCWS-ST	1.1	Flexure	60.3	61.8	41.6	0.98	1.45

Table 5. Comparison of Embedment Lengths for Test Specimens

Source	Specimen ID	Calculated L_e (in.)		
		Current Equation	Revised Equation	% Increase
Mattock and Gaffar (1982)	W4	7	15	114%
Kunwar and Shahrooz (2023)	SK-1	7	14	100%
	SK-2	9	17	89%
	SK-3	12	17	42%
	SK-4	12	16	33%
	SK-5	18	24	33%
	SK-6	20	29	45%
	SK-7	17	23	35%
Park et al. (2005)	SCB-ST	16	22	38%
	HCWS-ST	15	22	47%

through numerical simulations of more than 12,000 cases. Moreover, the embedment lengths determined from the revised and current equations were compared.

Based on Test Results

Using the dimensions and measured properties provided in Table 2, the nominal shear strengths, V_n, were computed from the revised equation (Equation 2) and the current AISC 341-22, Equation H4-4 (Equation 1). The results are compared against their experimental counterparts in Table 4. The nominal strengths instead of reduced design strengths, ϕV_n, are compared because the test specimens had been fabricated under controlled conditions, the as-built dimensions and measured material properties were used in the calculations, and the loading was well defined and known *a priori*. There is no obvious correlation between whether the coupling beam is shear/flexure critical and if the measured strength is overestimated or underestimated by the current equation. For example, specimens SK1 to SK4 were flexure controlled; however, SK1 and SK2 could develop V_n calculated from the current equation but SK3 and SK4 could not. None of the shear-controlled specimens could reach the V_n from the current equation. A common factor is the embedment region "aspect ratio"—that is, L_e/d.

For specimens SK-1, SK-2, SCB-ST, and HCWS-ST with small values of L_e/d, the measured connection strength is

Table 6. Values for Parametric Cases

Variable	Range/Value
Size of coupling beam	W14×22 to W30×326 excluding sections heavier than 350 plf
Wall thickness, b_w	18 in. to 54 in. (2 in. increment) Ignore cases with $b_w/b_f > 2$
Span of coupling beam, g	4 ft to 10 ft (1 ft increment)
Concrete compressive strength, f'_c	4 to 10 ksi (1 ksi increment)
Design shear, V	Smaller of $0.95(2\phi_b M_n/g$ and $\phi_v V_n)$ with no R_y
Wall transverse reinforcement	#5 with ¾ in. cover
Wall longitudinal reinforcement	#10

nearly equal to or larger than the nominal shear strength calculated by either the current or revised equation. It is reemphasized that the underlying assumption (a linear strain distribution over the embedment length) used for the derivation of both equations is not appropriate when L_e/d is small. The current equation, on the other hand, overestimates the measured connection strength (i.e., it underestimates the embedment length required to develop V_n) in 6 out of 10 cases with L_e/d greater than 1.1, including specimen W4 used by Mattock and Gaffar (1982) in the derivation of the current equation. The average value of $V_{test}/V_{n,current\ Eq.}$ is 0.81 with a coefficient of variation of 0.093. In contrast, the revised equation provides reasonable and conservative values. All the strength ratios from the revised equation are greater than 1. For the cases with L_e/d greater than 1.1, the average value of test/calculated nominal connection shear strength is 1.19 with a coefficient of variation equal to 0.18.

The required embedment lengths to develop the measured connection strengths (V_{test} shown in Table 4) were computed by using the current Equation 1 and the revised Equation 2 and are compared in Table 5. The calculated embedment lengths were rounded to the nearest in. Compared to the existing equation, the embedment length from the revised is, on average, 50% longer for cases with L_e/d greater than 1.1.

Based on Numerical Simulations

The revised equation was further evaluated numerically by considering a wide range of the key parameters: b_f, b_w/b_f, f'_c, and g. For this purpose, a total of 12,054 cases were selected based on the variables shown in Table 6. For a given wall thickness, the beam sizes were selected such that there would be a minimum of a 1 in. gap on either side of the beam flange and wall longitudinal bars. This gap is somewhat arbitrary but is the same as the value in ACI 318-19 for the minimum distance between longitudinal bars to ensure concrete consolidation. The concrete compressive strength was capped at 10 ksi to be consistent with the current AISC limit.

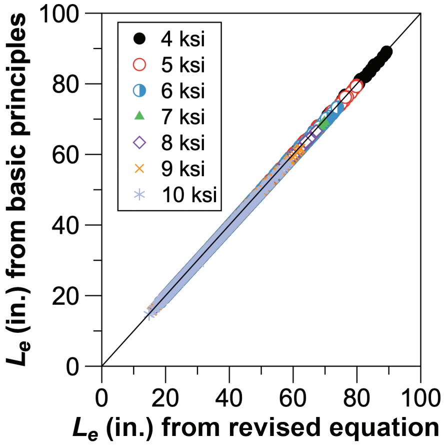

Fig. 3. Embedment length calculated from basic principles and revised equation.

The model shown in Figure 1 was used with the same assumptions used for derivation of Equation 2: (1) ε_f was set equal to 0.0038 and (2) spreading of bearing stresses was taken into account by multiplying the flange width by a taken as the lesser of 1.3 and b_w/b_f. The values of the depth of the neutral axis, c, and embedment length, L_e, were iterated to maintain equilibrium for a given value of design shear taken as the smaller of $0.95(2\phi_b M_n/g$ and $\phi_v V_n)$.

The analyses indicate that c/L_e ranges between 0.53 and 0.64, but Equation 2 was developed based on setting c/L_e equal to 0.57. This difference does not noticeably affect the calculated embedment lengths as evident from Figure 3, which compares the embedment length determined from basic principles (i.e., satisfying equilibrium of forces and moment by iterating the values of c and L_e) and the value calculated from Equation 2. Out of 12,504 cases, the embedment length determined from basic principles is longer than the value determined from Equation 2 for 91, 32, 14, 5, and 5 cases with f_c' equal to 4 ksi, 5 ksi, 6 ksi, 7 ksi, and 8 ksi, respectively. The largest difference is 0.82% for a case involving a 4-ft-long W18×311 beam used to couple 4 ksi wall piers. The application of such a heavy section to couple 4 ksi wall piers is not considered to be likely. The revised equation is, hence, deemed to be applicable for a wide range of cases encountered in practice.

The application of AISC 341-22, Equation H4-4 (Equation 1), to cases with relatively high concrete strengths is somewhat questionable considering the value of f_c' was 2.95 ksi for the only W-shape section used in the original research (Mattock and Gaffar, 1982). The current equation has been examined in several research programs with larger values of f_c', but the connection strength was not the controlling failure mode, the value of L_e/d was such that the underlying assumption of linear strain distribution along embedment length would not be accurate, or the connection strength was found to be less than the target strength. Nevertheless, the embedment lengths for the aforementioned 12,504 cases were calculated by the current equation, Equation 1, and the revised Equation 2, and the results were compared.

The histogram of the ratio of embedment length, L_e, from the revised equation divided by that from the current equation is plotted in Figure 4. On average, the embedment length calculated from the revised equation is 1.15 times longer than that from the current equation with a coefficient of variation of 0.078. The revised equation results in a maximum of 37% longer embedment length compared to the current equation. The embedment length from the current equation is slightly longer than that from the revised equation for a limited number of cases involving large concrete compressive strengths: 0.08%, 0.74%, and 2.54% of the number of cases with $f_c' = 8$ ksi, 9 ksi, and 10 ksi, respectively. However, the ratio of L_e from the revised equation to that from the current equation is 0.97 or larger for 99.2% of the total number of cases.

In addition to concrete compressive strength, the value of b_w/b_f, the coupling beam unit weight, and the expected yielding sequence (shear-critical, flexure-critical, or simultaneous yielding in flexure and shear) affect the relative magnitudes of embedment length from the revised and current equations, as evident from Figure 5. The ratio of embedment length from the revised equation to the length from the current equation drops below 1 for cases with f_c' exceeding 8 ksi, and as b_w/b_f becomes small, the coupling beam becomes heavier, and the coupling beam is shear critical (i.e., $g \leq 1.6M_p/V_p$) or is expected to yield in flexure and shear simultaneously (i.e., $1.6M_p/V_p < g < 2.6M_p/V_p$). It is noted again that the application of the current equation to cases with large values of f_c' is questionable.

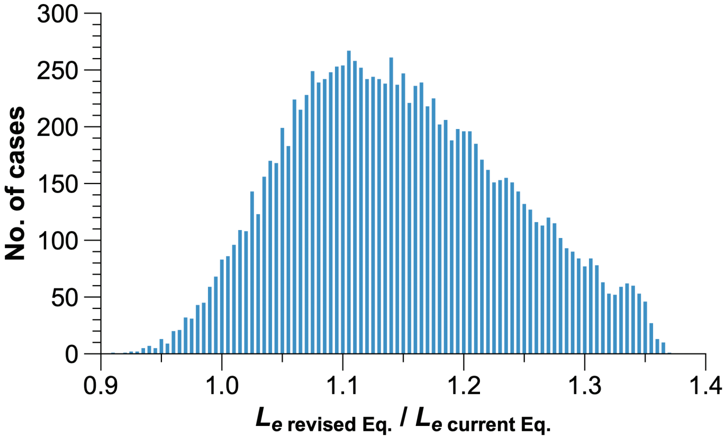

Fig. 4. Comparison of embedment lengths.

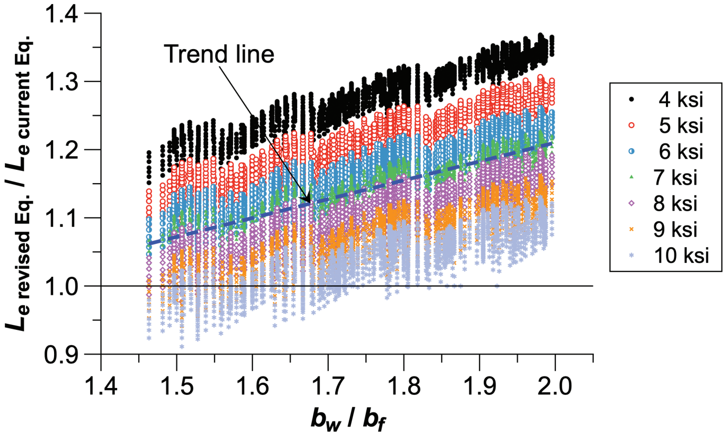

(a) *Influence of* b_w/b_f

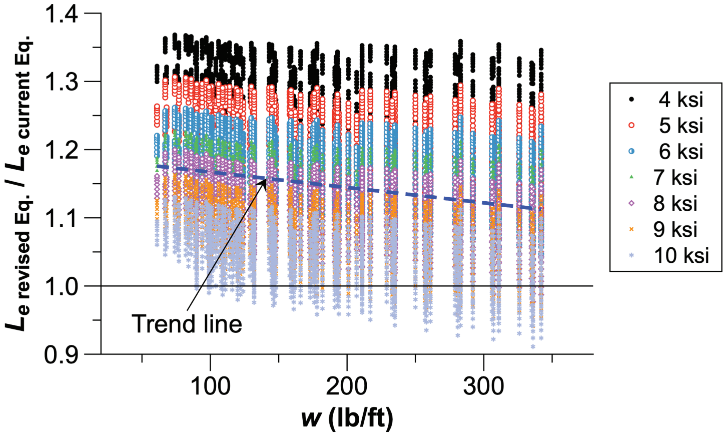

(b) Influence of coupling beam weight/foot

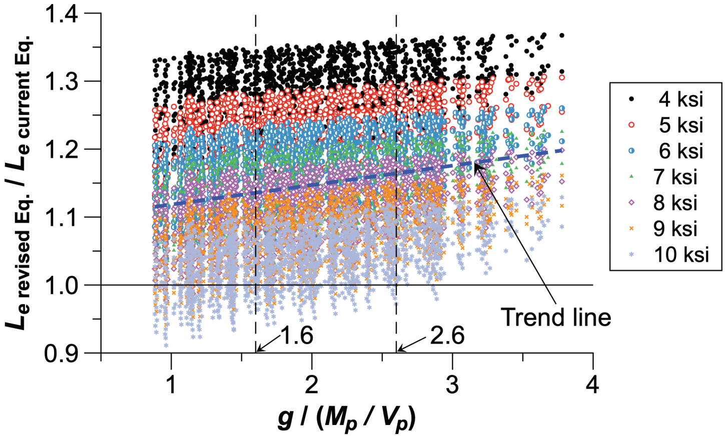

(c) Influence of yielding sequence

Fig. 5. Influence of various parameters on embedment length from revised equation vs. current equation.

CONCLUSION

Recent tests focused on steel coupling beams in composite ordinary shear walls (C-OSW) demonstrated the target strength could not be developed for several test specimens designed according to the current embedment length equation in AISC 341-22. A revised equation was developed and evaluated by using basic principles in conjunction with available test data. The equation was further validated through numerical simulations. The revised equation results in longer embedment lengths by as much as nearly 40% for cases that would likely be encountered in practice. The longer embedment length will ensure that the design loads can be developed prior to connection failure in the embedded region. The revised equation presented herein as Equation 2 is being considered as a replacement for the current AISC 341-22, Equation H4-4.

ACKNOWLEDGMENTS

The research presented in this report was funded by the Charles Pankow Foundation and co-funded by the American Institute of Steel Construction and the Magnusson Klemencic Associates (MKA) Foundation. The views presented in this paper are of the authors and do not represent the funding agencies' views. The authors dedicate this paper to our friend and colleague, Dr. Patrick J. Fortney at the University of Cincinnati, who unexpectedly passed away in 2019. His deep desire to understand the behavior and performance of ordinary composite coupled walls was the genesis of the reported research.

REFERENCES

ACI (2019), *Building Code Requirements for Structural Concrete*, ACI 318-19R and commentary, Farmington Hills, Mich.

AISC (2022), *Seismic Provisions for Structural Steel Buildings*, ANSI/AISC 341-22, American Institute of Steel Construction Chicago, Ill.

Fortney, J.P. (2005), "The Next Generation of Coupling Beams," PhD Dissertation, University of Cincinnati, Cincinnati, Ohio.

Harries, K.A. (1995), "Seismic Design and Retrofit of Coupled Walls Using Structural Steel," PhD Dissertation, McGill University, Montreal, Quebec, Canada.

Hognestad, E. (1951), "A Study of Combined Bending Axial Load in Reinforced Concrete Members," Bulletin Series No. 399, Engineering Experimental Station, University of Illinois, Urbana, Ill.

Kunwar, S. and Shahrooz, B.M. (2023), "Steel Coupling Beams in Low-Seismic and Wind Applications," Final Report to the Charles Pankow Foundation.

Marcakis, K. and Mitchell, D. (1980), "Precast Concrete Connections with Embedded Steel Members," *PCI Journal*, Vol. 25, No. 4, pp. 88–116.

Mattock, A.H. and Gaafar, G.H. (1982), "Strength of Embedded Steel Sections as Brackets," *ACI Structural Journal*, Vol. 79, No. 2, pp. 83–93.

Park, W.S. and Yun, H.D. (2006), "Seismic Performance of Steel Coupling Beam–Wall Connections in Panel Shear Failure," *Journal of Constructional Steel Research*, Vol. 62, pp. 1,016–1,025.

Park, W.S., Yun, H.D., Hwang, S.K., Han, B.C., and Yang, I.S. (2005), "Shear Strength of the Connection between a Steel Coupling Beam and a Reinforced Concrete Shear Wall in a Hybrid Wall System," *Journal of Constructional Steel Research*, Vol. 61, pp. 912–941.

Shahrooz, B.M., Fortney, P.J., and Harries, K.A. (2018), "Steel Coupling Beams with a Replaceable Fuse," *Journal of Structural Engineering*, ASCE, Vol. 144, No. 2, 04017210_1:11.

Shahrooz, B.M., Remmetter, M.E., and Qin, F. (1993), "Seismic Design and Performance of Composite Coupled Walls," *Journal of Structural Engineering*, ASCE, Vol. 119, No. 1, pp. 3,291–3,309.

Revisiting the P-δ Magnification Factor for Members Subject to End Moments

ERIC M. LUI

ABSTRACT

The 2022 edition of the AISC *Specification for Structural Steel Buildings* allows member and system instability effects to be accounted for by using advanced analysis methods that model these effects directly or through the use of the B_1 (P-δ) and B_2 (P-Δ) multipliers. For compression members subject to end moments only, the B_1 multiplier is expressed as a function of the smaller to larger end moment ratio. This ratio is taken as positive when the member bends in reverse curvature and negative when it bends in single curvature. This code equation for B_1 often overestimates the P-δ effect for double curvature bending under a high axial force but underestimates the P-δ effect for single curvature bending under almost all values of axial force. The reason for the overestimation is because the derivation of the B_1 equation uses the equivalent moment concept and ignores the actual location where the maximum moment occurs in the member. When this condition is taken into consideration, it is shown herein that the equation is no longer applicable for members bent in reverse curvature under any value of axial force. The reason for the underestimation is because the effect of axial force on the moment ratio is ignored. By incorporating this effect in a new equation for B_1, it is shown that this underestimation is drastically reduced. The validity of this proposed B_1 multiplier is established by comparison with the corresponding theoretical values.

Keywords: P-δ effect, B_1 factor, design equation.

INTRODUCTION

When a structural member is subject to the combined actions of compressive axial force and bending moments as shown in Figure 1, the lateral deflection and moment in the member will be magnified from their respective first-order values. The increase is the result of the axial force acting through the deflection of the member away from its chord (i.e., P-δ effect) and the same axial force acting on the relative deflection of one end of the member with respect to the other end (i.e., P-Δ effect).

To account for these two instability effects, the 2022 edition of the AISC *Specification for Structural Steel Buildings* (AISC, 2022), hereafter referred to as the AISC *Specification*, allows designers to use either a second-order elastic analysis that explicitly models these effects or an approximate second-order analysis that makes use of results obtained from a first-order elastic analysis in conjunction with two multipliers, B_1 and B_2. For moment and axial force, the equations that can be used are given by AISC *Specifications* Equations A-8-1 and A-8-2, and reproduced here as Equations 1a and 1b:

$$M_r = B_1 M_{nt} + B_2 M_{lt} \tag{1a}$$

$$P_r = P_{nt} + B_2 P_{lt} \tag{1b}$$

where

M_r = required second-order flexural strength using LRFD or ASD load combinations, kip-in. (N-mm)

P_r = required second-order axial strength using LRFD or ASD load combinations, kips (N)

M_{nt} = first-order moment obtained using the LRFD or ASD load combinations, when the structure is restrained against lateral translation, kip-in. (N-mm)

M_{lt} = first-order moment obtained using the LRFD or ASD load combinations, due to lateral translation, kip-in. (N-mm)

P_{nt} = first-order axial force obtained using the LRFD or ASD load combinations, when the structure is restrained against lateral translation, kips (N)

P_{lt} = first-order axial force obtained using the LRFD or ASD load combinations, due to lateral translation, kips (N)

B_1 = multiplier to account for the P-δ effect

B_2 = multiplier to account for the P-Δ effect

B_1 and B_2 are given by AISC *Specification* Equations A-8-3 and A-8-6, and are reproduced as Equations 2a and 2b:

Eric M. Lui, Meredith Professor, Department of Civil and Environmental Engineering, Syracuse University, Syracuse, N.Y. Email: emlui@syr.edu

---

Paper No. 2024-16

$$B_1 = \frac{C_m}{1 - \dfrac{\alpha P_r}{P_{e1}}} \geq 1 \tag{2a}$$

$$B_2 = \frac{1}{1 - \dfrac{\alpha P_{story}}{P_{e\,story}}} \geq 1 \tag{2b}$$

where α is taken as 1 for LRFD and 1.6 for ASD; P_{e1} is the elastic critical buckling strength of the member in the plane of bending, assuming the member ends do not undergo any lateral translation, kips (N); P_{e1} is given by AISC *Specification* Equation A-8-5 and is equal to $\pi^2 EI^*/(L_{c1})^2$, where EI^* is the flexural rigidity in kip-in.^{2} (N-mm^2), taken as $0.8\tau_b EI$ when used in the direct analysis method of design (AISC *Specification* Section C1.1) or as EI when used in the effective length and first-order analysis method of design (AISC *Specification* Section C1.2, Appendix 7); τ_b is the stiffness reduction parameter discussed in AISC *Specification* Section C2.3; L_{c1} is taken as the laterally unbraced length of the member in the plane of bending, in, (mm); P_{story} is the total vertical load acting on the story under consideration using LRFD or ASD load combinations, kips (N); and $P_{e\,story}$ is the elastic critical bucking strength of the story in the direction of lateral translation being considered, kips (N), determined by sidesway buckling analysis, or by AISC *Specification* Equation A-8-7.

C_m is the equivalent uniform moment factor, assuming the member ends undergo no lateral translation relative to each other. For members not subjected to transverse loading between the two member ends, the equation for C_m is given by AISC *Specification* Equation A-8-4, and reproduced below as

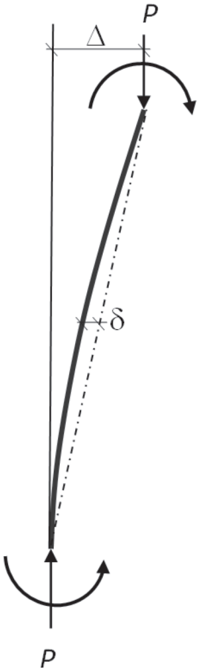

Fig. 1. P-delta effects.

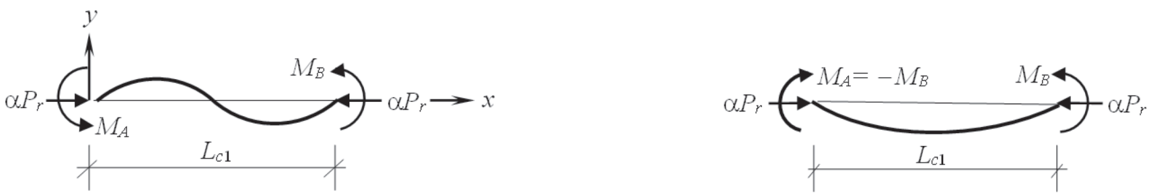

(a) End moments applied in the same direction

(b) End moments applied in equal and opposite directions

Fig. 2. Prismatic member subject to end moments and a compressive axial force.

$$C_m = 0.6 - 0.4\left(\frac{M_A}{M_B}\right) \tag{3}$$

in which M_A/M_B is the ratio of the smaller to larger end moments calculated using a first-order elastic analysis. M_A/M_B is taken as positive if the member bends in reverse curvature and negative if the member bends in single curvature. This equivalent moment factor allows the maximum moment in a member under end moments M_A and M_B shown in Figure 2(a) to be calculated from the maximum moment of a member subject to a pair of equal and opposite end moments shown in Figure 2(b).

Equation 3 was proposed by Austin (1961). The derivation of this equation can be found in Chen and Lui (1987). The Austin equation is a simplification of the equation

$$C_m = \sqrt{\frac{\left(\frac{M_A}{M_B}\right)^2 + 2\left(\frac{M_A}{M_B}\right)\cos\left(\pi\sqrt{\frac{\alpha P_r}{P_{e1}}}\right) + 1}{2\left(1 - \cos\pi\sqrt{\frac{\alpha P_r}{P_{e1}}}\right)}} \tag{4}$$

Note that Equation 4 is a function of both the moment ratio M_A/M_B and $\alpha P_r/P_{e1}$. Not accounting for this axial force effect makes Equation 3 less accurate (Ballio and Mazzolani, 1983; Duan et al., 1989; Chen and Shen, 2015). Over the years, researchers have studied this C_m factor (Massonnet, 1959; Chen and Zhou, 1987; Sohal and Syed, 1992; Chen and Wang, 1999), and simplifying equations have been proposed for use in design. However, one aspect of Equation 3, as well as with Equation 4 from which Equation 3 was derived, that many researchers have overlooked is that they do not take into consideration the actual location of the maximum bending moment (when acting in conjunction with an axial force) within in the member. If the location of this maximum bending moment does not fall within the physical length of the member (as will be shown mathematically in a later section), both equations become invalid and should not be used. Addressing these two issues (axial force effect on C_m and applying Equations 3 and 4 when they are not applicable) are the primary goals of this paper.

THEORETICAL BACKGROUND

In Figure 2(a), a prismatic structural member laterally braced at the ends without experiencing any relative end translations in the y-direction is subject to end moments M_A and M_B ($\geq M_A$) and a compressive axial force αP_r. The differential equation governing its behavior can be written as

$$\frac{d^2y}{dx^2} + \left(\frac{\alpha P_r}{EI^*}\right)y = \left(\frac{M_A + M_B}{EI^*}\right)\left(\frac{x}{L_{c1}}\right) - \left(\frac{M_A}{EI^*}\right) \tag{5}$$

where EI^* and L_{c1} are defined as before in Equation 2a.

The solution to this differential equation after enforcing the boundary conditions $y(0) = y(L) = 0$ is

$$y = -\left\{\frac{\left[\left(\frac{M_A}{M_B}\right)\cos\left(\pi\sqrt{\frac{\alpha P_r}{P_{e1}}}\right) + 1\right]}{\sin\left(\pi\sqrt{\frac{\alpha P_r}{P_{e1}}}\right)}\sin\left(\pi\sqrt{\frac{\alpha P_r}{P_{e1}}}\frac{x}{L_{c1}}\right) - \left(\frac{M_A}{M_B}\right)\left[\cos\left(\pi\sqrt{\frac{\alpha P_r}{P_{e1}}}\frac{x}{L_{c1}}\right) - 1\right] - \left(\frac{M_A}{M_B} + 1\right)\left(\frac{x}{L_{c1}}\right)\right\}\left(\frac{M_B}{\alpha P_r}\right) \tag{6}$$

And upon taking derivatives, one obtains

$$\frac{d^2y}{dx^2} = \left\{\frac{\left[\left(\frac{M_A}{M_B}\right)\cos\left(\pi\sqrt{\frac{\alpha P_r}{P_{e1}}}\right) + 1\right]}{\sin\left(\pi\sqrt{\frac{\alpha P_r}{P_{e1}}}\right)}\sin\left(\pi\sqrt{\frac{\alpha P_r}{P_{e1}}}\frac{x}{L_{c1}}\right) - \left(\frac{M_A}{M_B}\right)\cos\left(\pi\sqrt{\frac{\alpha P_r}{P_{e1}}}\frac{x}{L_{c1}}\right)\right\}\left(\frac{M_B}{EI^*}\right) \tag{7}$$

$$\frac{d^3y}{dx^3} = \left\{\frac{\left[\left(\frac{M_A}{M_B}\right)\cos\left(\pi\sqrt{\frac{\alpha P_r}{P_{e1}}}\right) + 1\right]}{\sin\left(\pi\sqrt{\frac{\alpha P_r}{P_{e1}}}\right)}\cos\left(\pi\sqrt{\frac{\alpha P_r}{P_{e1}}}\frac{x}{L_{c1}}\right) + \left(\frac{M_A}{M_B}\right)\sin\left(\pi\sqrt{\frac{\alpha P_r}{P_{e1}}}\frac{x}{L_{c1}}\right)\right\}\left(\frac{\pi}{L_{c1}}\sqrt{\frac{\alpha P_r}{P_{e1}}}\right)\left(\frac{M_B}{EI^*}\right) \tag{8}$$

The equation to determine the location where maximum moment occurs, denoted herein as $\tilde{x}$, can be obtained by setting Equation 8 equal to zero; that is,

$$\tan\left(\pi\sqrt{\frac{\alpha P_r}{P_{e1}}}\frac{\tilde{x}}{L_{c1}}\right) = \frac{-\left(\frac{M_A}{M_B}\right)\cos\left(\pi\sqrt{\frac{\alpha P_r}{P_{e1}}}\right) - 1}{\left(\frac{M_A}{M_B}\right)\sin\left(\pi\sqrt{\frac{\alpha P_r}{P_{e1}}}\right)} \tag{9}$$

It is important to note that the location for maximum moment $\tilde{x}$ determined from Equation 9 must fall in the range $0 \leq \tilde{x} \leq L_{c1}$, or $0 \leq (\tilde{x}/L_{c1}) \leq 1$, to ensure that the maximum moment occurs within the physical length of the member.

Table 1. Values of $\tilde{x}/L_{c1}$

		$\alpha P_r/P_{e1}$				
		0.1	**0.3**	**0.5**	**0.7**	**0.9**
M_A/M_B	–1.0	0.500	0.500	0.500	0.500	0.500
	–0.8	0.704	0.555	0.525	0.511	0.503
	–0.6	0.935	0.623	0.555	0.525	0.507
	–0.4	1.17	0.705	0.594	0.543	0.512
	–0.2	1.39	0.803	0.644	0.566	0.518
	0	1.58	0.913	0.707	0.598	0.527
	0.2	–1.43	–0.796	–0.626	–0.553	–0.514
	0.4	–1.31	–0.681	–0.528	–0.486	–0.492
	0.6	–1.22	–0.577	–0.417	–0.387	–0.449
	0.8	–1.14	–0.488	–0.306	–0.250	–0.343
	1.0	–1.08	–0.413	–0.207	–0.098	–0.027

Table 2. Theoretical Moment Magnification Factor, $B_{1,theory}$

		$\alpha P_r/P_{e1}$				
		0.1	**0.3**	**0.5**	**0.7**	**0.9**
M_A/M_B	–1.0	1.14	1.53	2.25	3.94	12.42
	–0.8	1.05	1.39	2.03	3.55	11.18
	–0.6	1.00	1.26	1.82	3.16	9.94
	–0.4	1	1.14	1.61	2.78	8.70
	–0.2	1	1.06	1.42	2.40	7.46
	0	1	1.01	1.26	2.04	6.23
	0.2	1	1	1	1	1
	0.4	1	1	1	1	1
	0.6	1	1	1	1	1
	0.8	1	1	1	1	1
	1.0	1	1	1	1	1

Once $\tilde{x}$ is determined, the maximum moment M_{max} can be obtained by substituting $(\tilde{x}/L_{c1})$ into Equation 7 and multiplying the resulting equation by the flexural rigidity EI^* of the member. M_{max} so obtained is given by

$$\begin{aligned} M_{max} &= \left[\frac{\sqrt{\left(\dfrac{M_A}{M_B}\right)^2 + 2\left(\dfrac{M_A}{M_B}\right)\cos\left(\pi\sqrt{\dfrac{\alpha P_r}{P_{e1}}}\right) + 1}}{\sin\left(\pi\sqrt{\dfrac{\alpha P_r}{P_{e1}}}\right)} \right] M_B = \qquad (10) \\ & B_{1,theory}\, M_B \end{aligned}$$

The term in brackets denoted as $B_{1,theory}$ is the theoretical elastic moment magnification factor. This factor accounts for the member instability (P-δ) effect that magnifies the primary moment acting on the member due to the presence of an axial force.

The equivalent moment factor C_m shown in Equation 4 is obtained by equating Equation 10 with the equation for M_{max} when $M_A = –M_B$ (i.e., when the member is subject to a pair of equal and opposite end moments).

Table 3. AISC *Specification* Moment Magnification Factor, $B_{1,AISC}$

		$\alpha P_r/P_{e1}$				
		0.1	**0.3**	**0.5**	**0.7**	**0.9**
M_A/M_B	−1.0	1.11	1.43	2.00	3.33	10.00
	−0.8	1.02	1.31	1.84	3.07	9.20
	−0.6	1	1.20	1.68	2.80	8.40
	−0.4	1	1.09	1.52	2.53	7.60
	−0.2	1	1	1.36	2.27	6.80
	0	1	1	1.20	2.00	6.00
	0.2	1	1	1.04	1.73	5.20
	0.4	1	1	1	1.47	4.40
	0.6	1	1	1	1.20	3.60
	0.8	1	1	1	1	2.80
	1.0	1	1	1	1	2.00

P-δ MOMENT MAGNIFICATION

The presence of a compressive axial force αP_r magnifies the larger of the two end moments (i.e., M_B). The magnification factor $B_{1,theory}$ given in Equation 10 can be used to magnify M_B only if $\tilde{x}$ satisfies the condition $0 \le (\tilde{x}/L_{c1}) \le 1$ to ensure that the maximum moment created by the combined actions of end moments and axial force falls within the physical length of the member. Values of $(\tilde{x}/L_{c1})$ for a range of M_A/M_B and $\alpha P_r/P_{e1}$ computed from Equation 9 are given in Table 1. The gray highlighted numbers mean the condition $0 \le (\tilde{x}/L_{c1}) \le 1$ is violated. Note that $\tilde{x}/L_{c1}$ does not fall within the physical length of the member when $M_A/M_B > 0$ (i.e., when the member bends in reverse curvature) and when $\alpha P/P_{e1}$ is small for certain values of $M_A/M_B < 0$ (i.e., for certain values of moment ratio when the member bends in single curvature).

By enforcing the condition $0 \le (\tilde{x}/L_{c1}) \le 1$, the theoretical values of the moment magnification factor $B_{1,theory}$ calculated from Equation 10 are given in Table 2. Because the condition $0 \le (\tilde{x}/L_{c1}) \le 1$ is violated in the gray-shaded area, the maximum moment acting on the member is therefore taken as the larger of the two end moments (i.e., M_B), so the moment magnification factor is set equal to 1.

When Equation 3 is substituted into Equation 2a, the AISC *Specification* moment magnification factor ($B_{1,AISC}$) for members subject to end moments M_A and M_B and an axial compressive force αP_r can be written as

$$B_{1,AISC} = \frac{0.6 - 0.4\left(\dfrac{M_A}{M_B}\right)}{1 - \dfrac{\alpha P_r}{P_{e1}}} \ge 1 \tag{11}$$

Values of $B_{1,AISC}$ computed using this equation are given in Table 3. Upon comparison with Table 2, it can be seen that Equation 11 underestimates the moment magnification effect for almost all $\alpha P_r/P_{e1}$ when $M_A/M_B < 0$ (single curvature bending) but overestimates its effect for high $\alpha P_r/P_{e1}$ when $M_A/M_B > 0$ (double curvature bending) in the yellow-shaded area. More importantly, the numbers shown in the yellow-shaded area should not even be used since the condition $0 \le (\tilde{x}/L_{c1}) \le 1$ is violated as depicted in Table 1.

The moment magnification effect is underestimated because the term $\alpha P_r/P_{e1}$ is ignored in the numerator of Equation 11. To remedy this, a nonlinear regression analysis was performed on Equation 4, and a new equation for C_m is proposed as follows.

$$C_m = 0.6 - \left(0.4 + 0.25\frac{\alpha P_r}{P_{e1}}\right)\left(\frac{M_A}{M_B}\right) \tag{12}$$

Using this equation for C_m, the improved P-δ moment magnification factor is proposed as

$$B_{1,proposed} = \begin{cases} \dfrac{0.6 - \left(0.4 + 0.25\dfrac{\alpha P_r}{P_{e1}}\right)\left(\dfrac{M_A}{M_B}\right)}{1 - \dfrac{\alpha P_r}{P_{e1}}} \ge 1 & -1 \le \dfrac{M_A}{M_B} \le 0 \\ 1 & \text{otherwise} \end{cases} \tag{13}$$

Values of the moment magnification factor computed using Equation 13 are shown in Table 4. When compared to the theoretical values given in Table 2 and plotted together in Figure 3, good agreement is observed. The maximum error is less than 5%, which occurs at $\alpha P_r/P_{e1} = 0.9$.

Table 4. Proposed Moment Magnification Factor, $B_{1,proposed}$

		$\alpha P_r/P_{e1}$				
		0.1	**0.3**	**0.5**	**0.7**	**0.9**
M_A/M_B	−1.0	1.14	1.54	2.25	3.92	12.25
	−0.8	1.04	1.40	2.04	3.53	11.00
	−0.6	1	1.26	1.83	3.15	9.75
	−0.4	1	1.13	1.62	2.77	8.50
	−0.2	1	1	1.41	2.38	7.25
	0	1	1	1.20	2.00	6.00
	0.2	1	1	1	1	1
	0.4	1	1	1	1	1
	0.6	1	1	1	1	1
	0.8	1	1	1	1	1
	1.0	1	1	1	1	1

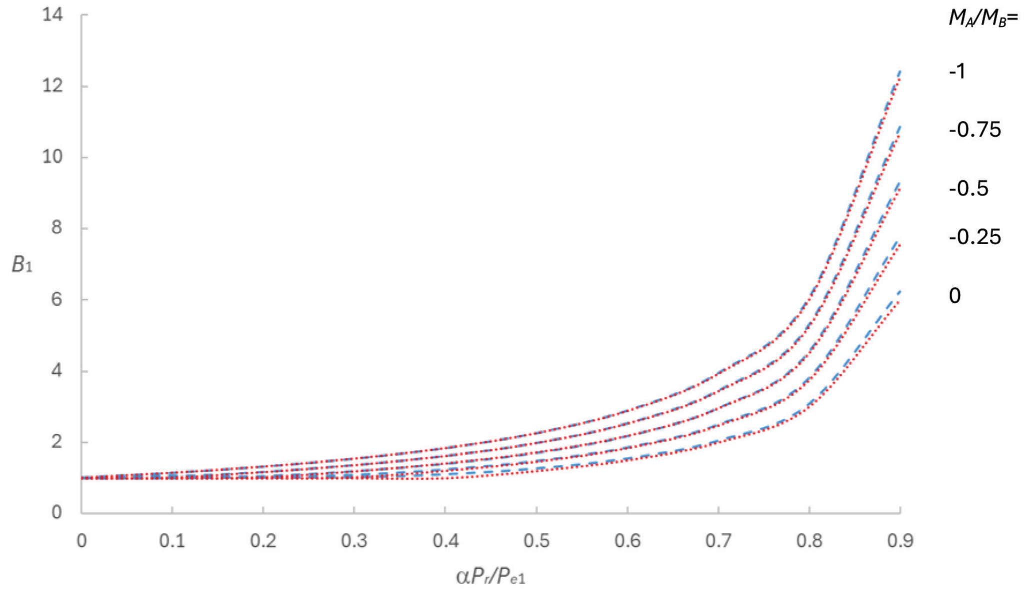

Fig. 3. Comparison of theoretical (blue dashed lines) and proposed (red dotted lines) moment B_1 *factor.*

CONCLUSIONS

When a member is subject to a pair of end moments and an axial compressive force, the end moments cause the member to deflect from its chord, and the axial force acts through this lateral deflection to produce additional moment in the member. This phenomenon is referred to as the P-δ effect. To account for this effect, the 2022 AISC *Specification* permits the use of a second-order analysis or the use of the P-δ moment magnification factor B_1. The current equation for B_1 has two fallacies: It does not take into account that the magnified moment may not occur within the physical length of the member, and it ignores the axial force effect in the numerator of the equation. In this paper, it is shown that the moment magnification effect does not apply to cases where the end moments cause the member to bend in reverse curvature; by introducing an axial force term in the numerator of the moment magnification equation, the P-δ effect can be more accurately represented. Comparison of B_1 values calculated using the proposed equation and their theoretical values show that the errors are well within 5%.

REFERENCES

AISC (2022), *Specification for Structural Steel Buildings*, ANSI/AISC 360-22, American Institute of Steel Construction, Chicago, Ill.

Austin, W.J. (1961), "Strength and Design of Metal Beam-Columns," *Journal of the Structural Division*, ASCE, Vol. 87(ST4), pp. 1–32.

Ballio, G. and Mazzolani, F.M. (1983), *Theory and Design of Steel Structures*, Chapman and Hall, London, UK.

Chen, S-F. and Shen, H-X. (2015), "Improved Accuracy for the C_m Factor of Steel Beam-Columns," *Engineering Structures*, Vol. 103, pp. 28–36.

Chen, S-J. and Wang, W-C. (1999), "Moment Magnification Factor for P-d Effect of Steel Beam-Columns," *Journal of Structural Engineering*, ASCE, Vol. 125, No. 2, pp. 219–233.

Chen, W.F. and Lui, E.M. (1987), *Structural Stability—Theory and Implementation*, Elsevier, New York, N.Y.

Chen, W.F. and Zhou, S.P. (1987), "C_m Factor in Load and Resistance Factor Design," *Journal of Structural Engineering*, ASCE, Vol. 118, No. 8, pp. 1,738–1,754.

Duan, L., Sohal, I.S., and Chen, W.F. (1989), "On Beam-Column Magnification Factor," *Engineering Journal*, AISC, Vol. 26, No. 4, pp. 130–135.

Massonnet, C. (1959), "Stability Considerations in the Design of Steel Columns," *Journal of the Structural Division*, ASCE, Vol. 85, pp. 75–111.

Sohal, I.S. and Syed, N.A. (1992), "Inelastic Amplification Factor for Design of Steel Beam-Columns," *Journal of Structural Engineering*, ASCE, Vol. 118, No. 7, pp. 1,822–1,833.

Steel Structures Research Update

Additive Manufacturing for Structural Steel Applications

JUDY LIU

INTRODUCTION

Research under way on large-format metallic additive manufacturing for structural steel applications is highlighted. Dr. Ryan Sherman, Associate Professor in the School of Civil and Environmental Engineering at the Georgia Institute of Technology, leads this study. Dr. Sherman's research on steel bridge and ancillary highway structures encompasses large-scale laboratory testing, field monitoring, material characterization, and finite element simulation. Research interests include fatigue, fracture, and additive manufacturing for civil engineering infrastructure. The Terry Peshia Early Career Faculty Award (AISC), the Robert J. Dexter Memorial Award Lecture (Steel Bridge Task Force), and Georgia Tech's Student Recognition of Excellence in Teaching are among Dr. Sherman's accolades. An AISC Milek Fellowship, awarded in 2023, supports this research, building on work with Lincoln Electric Additive Solutions and funded by the Federal Highway Administration (FHWA). As part of that effort, AISC Undergraduate Research Fellow Shirin Raschid Farrokhi investigated fatigue performance under the mentorship of PhD candidate Hannah Kessler. Kessler, the 2025 Reidar Bjorhovde Outstanding Young Professional recipient, also conducted tension, impact, and fatigue testing for the FHWA project and, with PhD student Zachary de Haaff, has been integral to the research team. Selected highlights from completed and planned research are presented.

BACKGROUND

Additive manufacturing (AM) presents opportunities for steel construction, but questions about material, connection, and component behavior and design must be addressed. Advantages for steel AM include automation and the ability to create and optimize complex geometries with reduced material waste. Such advantages have been demonstrated in aerospace, maritime, and other industries. Potential applications in steel construction range from new construction to repair and rehabilitation (Kessler and Sherman, 2025). Research is needed to address knowledge gaps and advance AM for structural steel applications.

The team has been researching wire arc AM (WAAM). WAAM is a directed energy deposition (DED) process that uses the same metallic wire feedstocks used for welding. A completed study has answered questions about material and fatigue behavior. Specifically, the team has created material property datasets for WAAM ER70S-6 and ER80S-Ni1 filler metal components through tension, Charpy V-notch (CVN) impact, and fatigue performance tests. They have studied the influence of the as-built, or as-fabricated, surface finish, as well as material property anisotropy with respect to build and deposition directions (Sherman et al., 2023, 2024).

The tension and impact test programs examined the effects of interpass temperature, orientation, and location within the AM build. The robotic welding arm deposited layers of metal horizontally and built vertically on those layers (Figure 1). Tension coupons from the AM build were parallel to the deposition direction (DD), parallel to the build direction (BD), and oriented at 45° (Figure 2). CVN specimens were parallel to the deposition direction or the build direction. CVN specimens were also located within the middle half-thickness (½ T) or at a quarter-thickness (¼ T), as shown in Figure 2. Relatively low and high interpass temperatures were studied. Details for the test programs may be found in Kessler and Sherman (2024, 2025).

Tension test results showed dependence on interpass temperature. Loading direction had little influence on strength. For both filler metal classifications and interpass temperatures, yield and tensile strengths did not exhibit any significant anisotropy. However, the percent elongation at fracture was affected by the load orientation. Results showed higher percentage elongation for gauge lengths and loading parallel to the deposition direction (DD) than those with gauge lengths and loading parallel to the build direction (BD) and at 45° between the BD and DD. Low interpass temperatures correlated to higher yield and tensile strengths than for the high interpass temperatures (Sherman et al., 2024). More results may be found in Kessler and Sherman (2024, 2025).

CVN impact test results exceeded ASTM A709/A709M Grade 50 (ASTM, 2024) limits for both members requiring

---

Judy Liu, PhD, Research Editor of the AISC *Engineering Journal*, Professor, Oregon State University, School of Civil and Construction Engineering, Corvallis, Ore. Email: judy.liu@oregonstate.edu

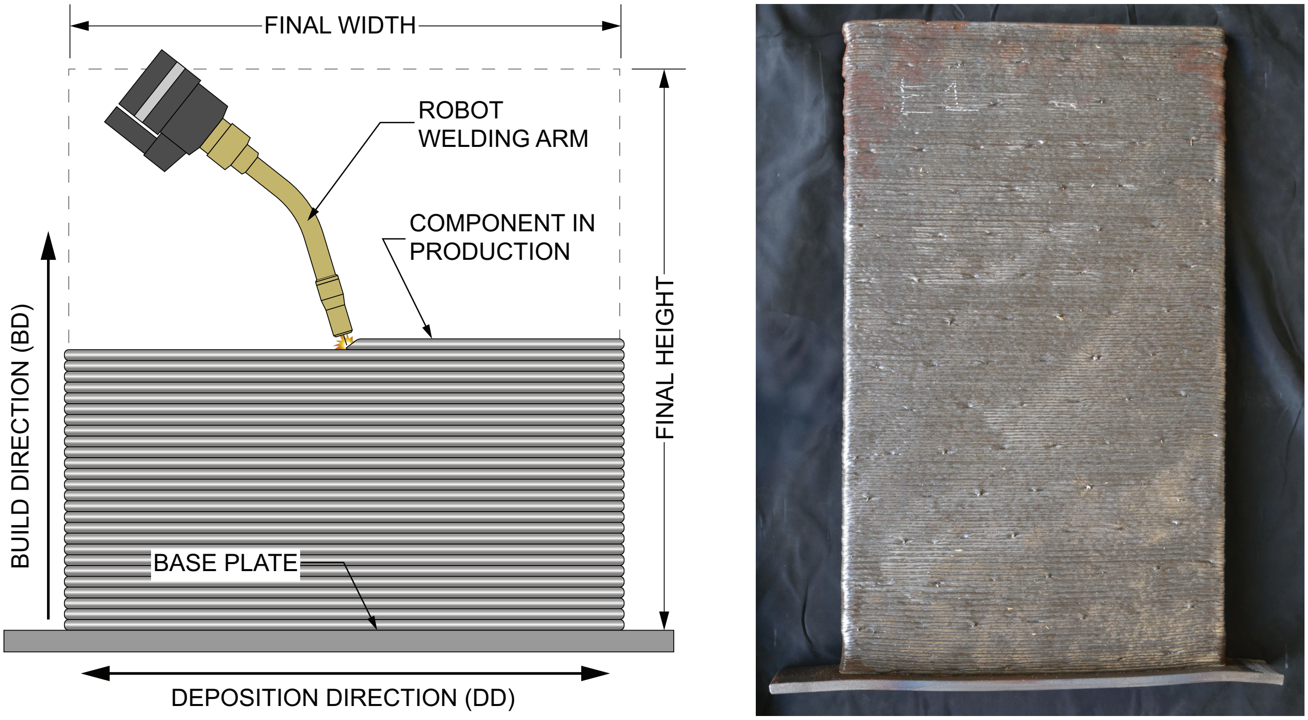

(a) Schematic

(b) Photograph

Fig. 1. Build and deposition direction.

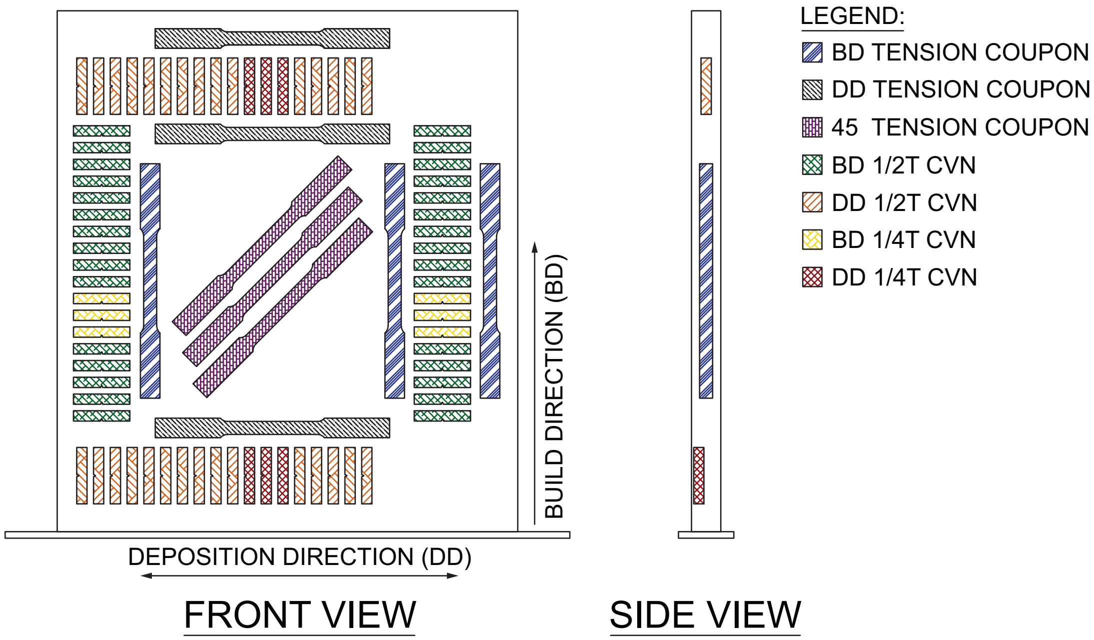

Fig. 2. Tension and CVN specimen orientations and locations through the thickness.

and not requiring fracture critical control practice for all service temperature zones (Sherman et al., 2024). More results may be found in Kessler and Sherman (2024, 2025).

The test program also addressed the knowledge gap for fatigue behavior of ER80S-Ni1 feedstock. Fatigue studies had been conducted for WAAM ER70S-6 (e.g., Sherman et al., 2023). ER80S-Ni1 has corrosion resistance to atmospheric weathering and is a matching feedstock for weathering steel applications such as bridges and other transportation infrastructure. The primary objectives of this study were to characterize fatigue behavior of WAAM ER80S-Ni1 for machined and as-built surface finishes at multiple interpass temperatures; to correlate fatigue life to fatigue detail categories from the AASHTO LRFD Bridge Design Specifications (2020); and to determine the influence of as-built, or as-fabricated, surface finish on fatigue performance. The AM build and fatigue specimens, with the as-built surface finish maintained or removed within the gauge length, are shown in Figure 3. Results showed machined specimen fatigue lives above the upper-bound curves for AASHTO detail Category A. For the as-built specimen, fatigue lives were between Categories C and D. There was no dependence on interpass temperatures for machined or as-built specimens. Given the clear dependence on surface finish, a machined surface finish was recommended for a higher level of fatigue performance (Farrokhi and Sherman, 2024; Kessler et al., 2025). AM builds with as-built surface finishes could also be sized for the desired stress range.

RESEARCH THEMES AND OBJECTIVES

The Milek Fellowship work continues research needed to realize the potential of large-format metallic additive manufacturing (AM) for structural steel applications. The two major themes for the research are connection considerations and component demonstration. For connections, the team is characterizing the behavior of bolted and welded AM connections, using component testing to establish mechanical properties as well as fatigue performance. Component demonstration will be through computational analyses and large-scale testing. The researchers will potentially examine structural steel applications such as an AM component or an AM repair.

The connection research objectives span strength limit states to fatigue performance. Small-scale component tests establish bolt bearing, tearout, and block shear rupture strengths. Testing of AM to base metal joints provides tensile and impact properties for multiple interpass temperatures. Fatigue tests quantify the performance of AM material and the influence of pretensioned high-strength bolts.

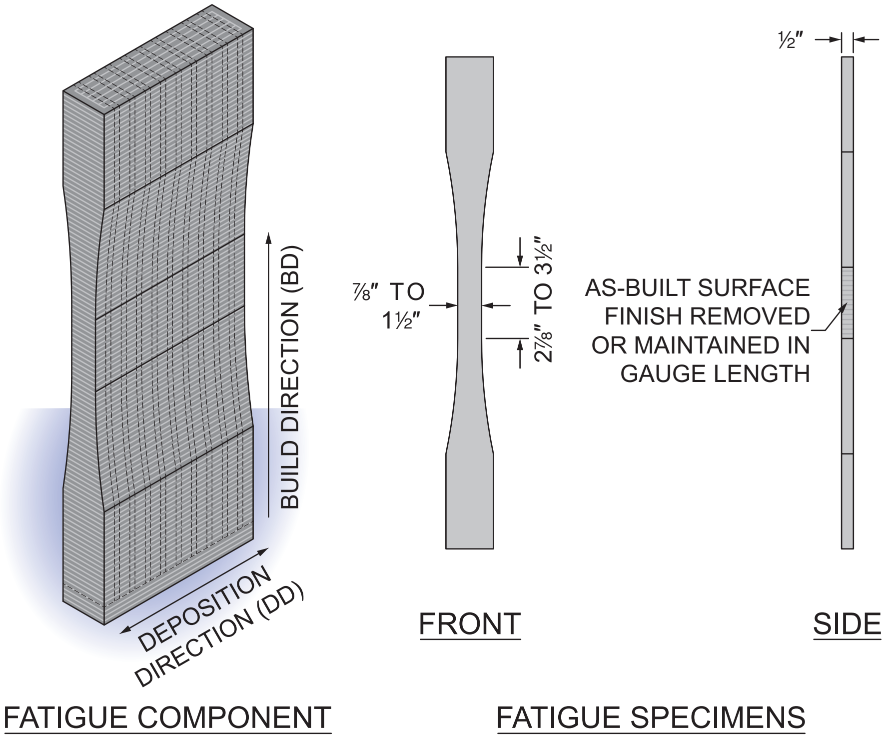

Fig. 3. Fatigue component fabrication schematic with specimen front and side views.

The component demonstration objectives focus on application and validation. The researchers seek to develop a model workflow to guide designers from concept to fabrication. Large-scale experimental testing will be used to validate design and performance of an optimized AM structural steel component or possibly an AM repair.

The research is organized into five primary tasks: bolted connection strength, welded joint properties, fatigue performance, model workflow development, and large-scale structural evaluation. At the time of writing, the work had been focused on experimental test program development for the first three tasks.

Bolted Connection Evaluation

Bolted connection limit states and AM parameters are studied. The test specimens are designed and detailed for the desired limit state—for example, net section rupture. Machined and as-built specimens are loaded parallel to the build or deposition direction.

The test setup simulates a tension member with a bolted connection. The hydraulic actuator and test frame impose uniaxial loading through double-shear connections to the specimen (Figure 4). The test area is the lower portion of the specimen, connected to the fixture base anchored to the strong floor. Instrumentation includes digital image correlation (DIC) on the test area.

The bolted connections are designed for the limit states of bolt bearing, bolt tearout, net section rupture, and block shear rupture. Connections for the WAAM ER70S-6 specimens use ⅞-in.-diameter ASTM F3125/F3125M Grade A325 (2025) bolts. The base module has overall dimensions of ½ in. × 6 in. × 12½ in. (Figure 5). The 15⁄16-in.-diameter bolt holes are located as needed for the desired limit state. The bearing and block shear specimens maintain the original 6 in. × 12½ in. geometry. For bearing, a single bolt hole is centered with a 2½ in. end distance. For block shear rupture, two bolts are symmetrically placed with 2½ in. spacing and a 2½ in. end distance. The tearout and net section rupture specimens use reduced sections for higher stresses in 3-in.-wide test areas. For the tearout specimen, the bolt hole is shifted closer to the end, with a distance of 1⅛ in. For net section rupture, the bolt hole is located 2 in. from the end.

In these tests, AM parameters investigated are surface finish and loading direction. Surface finish is either machined or as-built. Machined specimens are tested for all limit states. The machined specimens are built to a 1 in. thickness and machined to ½ in. thick. As-built specimens are also tested for the net section rupture. All specimens are tested for loading parallel to the build direction or to the deposition direction. There are three replicates for each combination of limit state, surface finish, and loading direction.

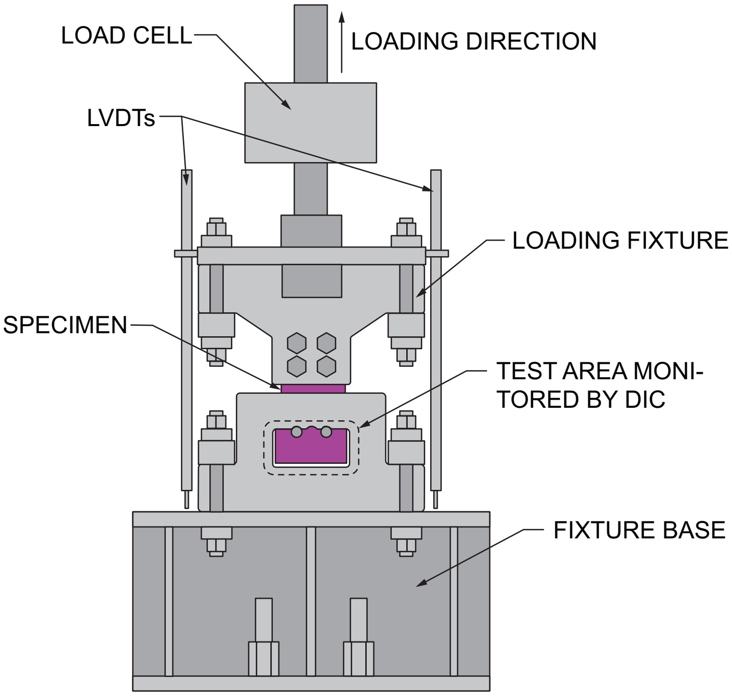

Fig. 4. Bolted connection test setup.

Welded Joint Evaluation

Tensile, CVN impact, and bend properties are evaluated for WAAM ER70S-6 builds welded to structural steel plates. The AM build direction is perpendicular to the weld to the ASTM A572/A572M Gr. 50 (2021c) plate (Figure 6). Two welded assemblies are planned; one AM build has a lower interpass temperature than the other.

Tensile properties are evaluated for different directions and locations in the welded assembly. The specimens, taken from the mid-thickness, are used to evaluate the tensile properties of the AM build, the A572 base metal, and the heat affected zone (HAZ) at the weld. Loading and specimen axis are parallel to the build direction or the deposition direction (Figure 6). Per assembly, there are three replicates for most combinations of specimen type (AM, base metal, HAZ) and build direction. The one exception is that there is only one HAZ specimen per plate in the deposition direction. The tensile test uses a universal testing machine (UTM), following ASTM E8 (2021a).

CVN impact properties are also evaluated. Most specimens are from mid-thickness (½T) of the assembly with some from the quarter thickness (¼T) location. The change in location is used to assess potential variation through the thickness. The specimens are sampled to test impact properties of the AM material, A572 base metal, and the HAZ. The specimen notches are broached at Georgia Tech to ensure they are within the HAZ. Per assembly, there are 15 tests for each combination of specimen type (AM, base metal, HAZ) and the ½T location. There are three tests per assembly for each specimen type and the ¼T location. Testing follows ASTM E23 (2018).

Bend tests are conducted on the welded joint builds. Specimens are from mid-thickness (½T) of the assembly. The specimens are sampled to test the bend properties of the face and side of the welded joint. There are three tests per assembly for each specimen type, face bend and side bend. Testing follows AWS D1.1 and D1.5 (2025a, 2025b).

Fatigue Performance Evaluation

Fatigue tests align with prior research and also explore the behavior of holes with and without bolts. Loading for all specimens is in the build direction. As-built and machined WAAM ER70S-6 specimens (Figure 7) are tested for stress ranges of 16–20 ksi and 30–38 ksi, respectively. Each combination of surface finish (as-built or machined) and stress range is tested with and without pretensioned, high-strength bolts. The as-built test combinations have three replicates; the machined tests are repeated for two replicates. The test procedure with the UTM follows the ASTM E466 (2021b).

Component Demonstration Research

With the unique AM opportunities for structural steel come challenges in predicting performance and establishing design procedures to meet specifications. The team plans to demonstrate the process with a computational parametric study and large-scale laboratory testing. Specifically, the demonstration includes a workflow model and laboratory testing of WAAM ER70S-6 structural steel applications.

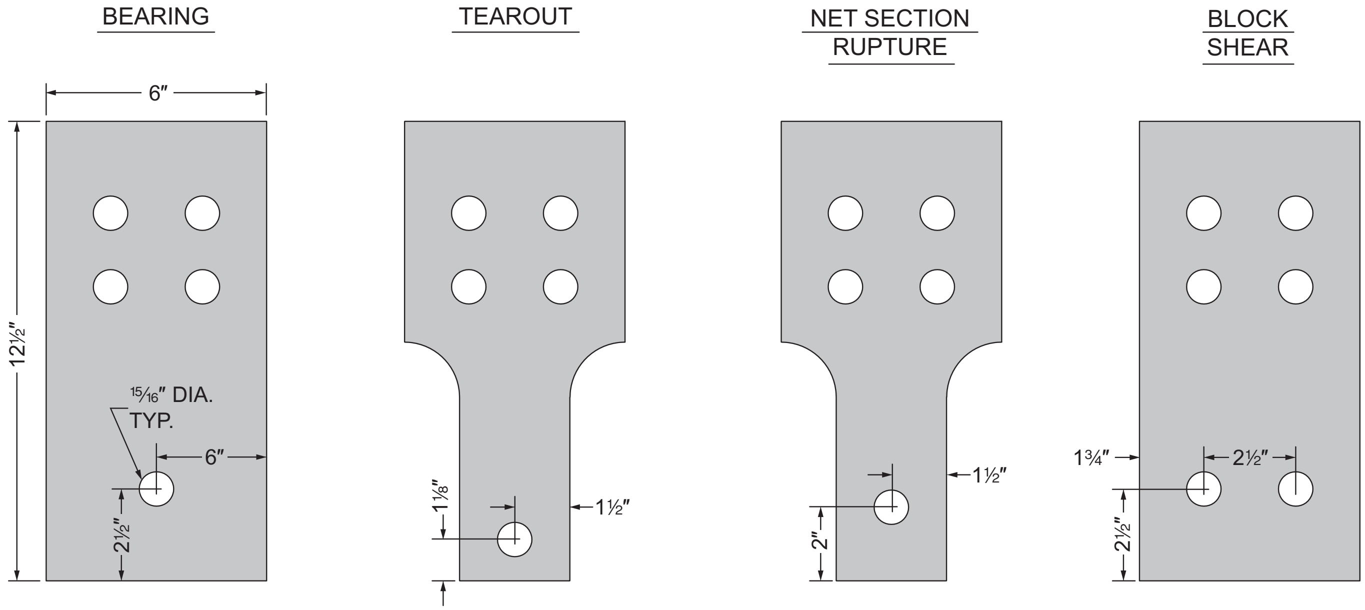

Fig. 5. Bolted connection specimens.

A model workflow delineates the design process. The freedom with AM necessitates new design guidance, tools, and methods beyond conventional prescriptive provisions for steel building and bridge design. Unique and potentially intricate geometries require finite element analysis (FEA) along with performance-based design provisions for schematic and design development. As a demonstration, the team plans to develop FEA and an optimization process for an AM structural steel component. Optimization of topology and shape may use objective functions such as minimizing strain energy or maximizing stiffness within a specified volume or weight of material. Results from the component evaluations inform material models used in the FEA.

Large-scale experimental evaluation will provide further demonstration of the process. Potential demonstration components include an AM beam-to-column connection node

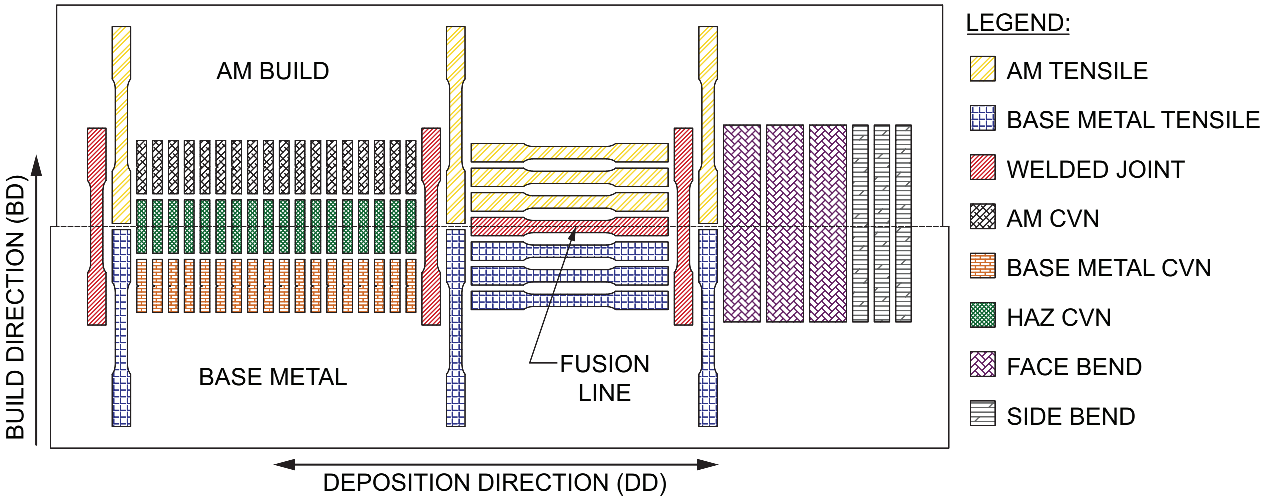

Fig. 6. Welded joint tensile and CVN specimen orientations and locations in AM build, steel base metal, and weld or HAZ.

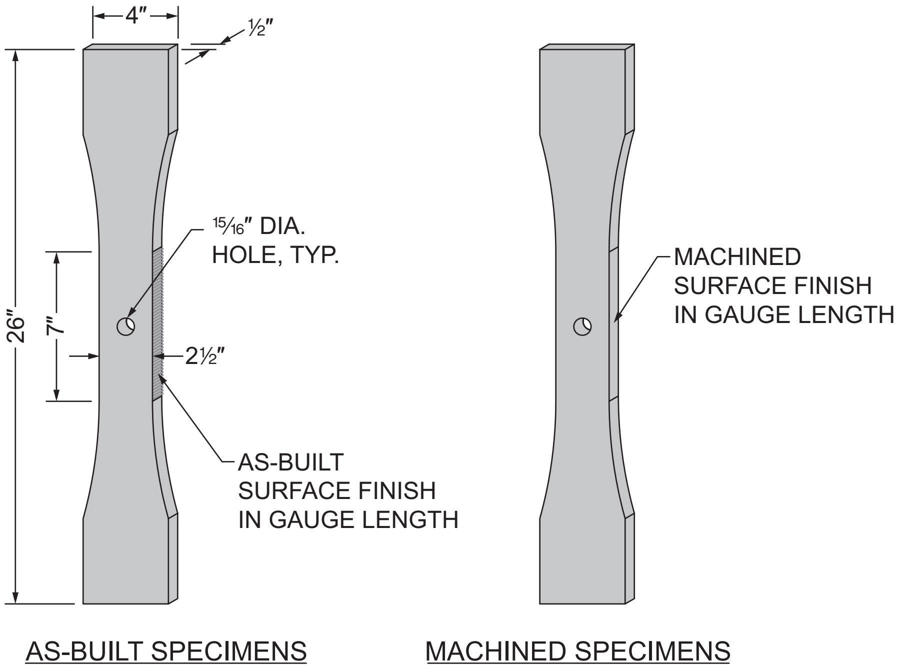

Fig. 7. Specimens with as-built and machined surfaces for fatigue performance tests.

and an AM corrosion repair of a beam end. Destructive testing results will be used to validate the design process.

An example of an ongoing, large-scale AM demonstration project is the AISC AM Pedestrian Bridge, featured at the 2025 NASCC in Louisville, Kentucky. As part of the AISC AM Exploratory Task Force, a range of structural steel industry stakeholders collaborated to design and fabricate a full-scale pedestrian bridge that highlights the opportunities AM provides the industry. The bridge merges traditional rolled steel products with the use of AM components, creating geometries and opportunities not feasible without AM. The research team at Georgia Tech will further this demonstration project by conducting controlled load testing of the AM bridge, helping to inform future integration into the steel industry.

INDUSTRY INVOLVEMENT AND EXPECTED OUTCOMES

Insights from industry experts throughout the project strengthen the impact of the research. Dr. Sherman serves as the chair of the AISC AM Exploratory Task Force, and the Milek Fellowship research team is advised by an industry oversight group. Fabricators, erectors, producers, engineers, researchers, and service providers in these groups provide insights and suggestions that guide research into practice. Research deliverables will include AM material and fatigue performance datasets, guidelines for bolted and welded connections, a model workflow, and large-scale AM demonstrations for new construction and repair. Among the expected benefits are innovative options for optimized and complex connection details, accelerated construction, repair and rehabilitation.

ACKNOWLEDGMENTS

Thank you to Dr. Ryan Sherman and PhD candidate Hannah Kessler for their many contributions to this article. The work of PhD student Zachary de Haaff and former undergraduate researcher Shirin Farrokhi is also acknowledged. The Federal Highway Administration (FHWA) supported the prior research under contract 693JJ321C00032. The Milek Fellowship research is funded by the American Institute of Steel Construction (AISC), with in-kind support provided by Lincoln Electric Additive Solutions. The researchers would also like to thank the AISC oversight committee: Joe Zona (Simpson Gumpertz & Heger Inc. Consulting Engineers), Brad Fletcher (Atlas Tube Inc.), Ronnie Medlock (High Steel Structures LLC), Lee Shoemaker (Metal Building Manufacturers Association, Thomas Associates, Inc.), Brian Volpe (Cives Engineering Corporation), Curtis Decker (Lincoln Electric), Carlos de Oliveira (Cast Connex), Devin Huber (AISC), Chris Garrell (National Steel Bridge Alliance), Luke Faulkner (AISC), Rob Connor (Purdue University), and Amit Kanvinde (University of California–Davis). Any findings or recommendations are those of the researchers and do not necessarily reflect the views of the sponsors.

REFERENCES

AASHTO (2020), *LRFD Bridge Design Specifications*, 8th Ed., American Association of State Highway and Transportation Officials, Washington, D.C.

ASTM (2018), *Test Methods for Notched Bar Impact Testing of Metallic Materials*, ASTM E23-18, ASTM International, West Conshohocken, Pa.

ASTM (2021a), *Test Methods for Tension Testing of Metallic Materials*, ASTM E8-21, ASTM International, West Conshohocken, Pa.

ASTM (2021b), *Standard of Practice for Conducting Force Controlled Constant Amplitude Axial Fatigue Tests of Metallic Materials*, ASTM E466-21, ASTM International, West Conshohocken, Pa.

ASTM (2021c), *Standard Specification for High-Strength Low-Alloy Columbium-Vanadium Structural Steel*, ASTM A572/A572M-21e1, ASTM International, West Conshohocken, Pa.

ASTM (2024), *Standard Specification for Structural Steel for Bridges,* ASTM A709/A709M, ASTM International, West Conshohocken, Pa.

ASTM (2025), *Standard Specification for High Strength Structural Bolts and Assemblies, Steel and Alloy Steel, Heat Treated, In. Dimensions 120 ksi, 144, ksi, and 150 ksi Minimum Tensile Strength, and Metric Dimensions 830 MPa and 1040 MPa Minimum Tensile Strength*, ASTM F3125/3125M, ASTM International, West Conshohocken, Pa.

AWS (2025a), *Structural Welding Code—Steel*, AWS D1.1/D1.1M:2025, American Welding Society, Miami, Fla.

AWS (2025b), *Bridge Welding Code*, AWS D1.5/D1.5M:2025, American Welding Society, Miami, Fla.

Farrokhi, S.R. and Sherman, R.J. (2024), "Understanding the Fatigue Behavior of Wire Arc Additively Manufactured Steel: Report of Fatigue Testing Results," Georgia Institute of Technology, Report to the American Institute of Steel Construction.

Kessler, H.D., Farrokhi, S.R., and Sherman, R.J. (2025), "Fatigue Performance of Wire Arc Additively Manufactured ER70S-6 and ER80S-Ni1," *Journal of Bridge Engineering*, ASCE, Vol. 30, No. 10. https://doi.org/10.1061/JBENF2.BEENG-7229.

Kessler, H.D. and Sherman, R.J. (2024), "Tension and Charpy V-Notch Impact Properties of Wire Arc Additively Manufactured ER80S-Ni1," *Structures,* Vol. 61, https://doi.org/10.1016/j.istruc.2024.106134.

Kessler, H.D. and Sherman, R.J. (2025), "Tension and Charpy V-Notch Impact Properties of Wire Arc Additively Manufactured ER70S-6," *Journal of Materials in Civil Engineering*, ASCE, Vol. 37, No. 5, https://doi.org/10.1061/JMCEE7.MTENG-1873.

Sherman, R.J., Kessler, H.D., Frank, K.H., and Medlock, R. (2023), "Evaluation of Large-Format Metallic Additive Manufacturing (AM) for Steel Bridge Applications: Final Report of Tensile, Impact, and Fatigue Testing Results," Georgia Institute of Technology, Atlanta, Ga.

Sherman, R.J., Kessler, H.D., Frank, K.H., and Medlock, R. (2024), "Evaluation of Large-Format Metallic Additive Manufacturing (AM) for Steel Bridge Applications [Tech Brief]," Federal Highway Administration, FHWA-HIF-24-008, Washington, D.C.

Guide for Authors

Scope *Engineering Journal* is dedicated to the improvement and advancement of steel construction. Its pages are open to all who wish to report on new developments or techniques in steel design, research, the design and/or construction of new projects, steel fabrication methods, or new products of significance to the uses of steel in construction. Only original papers should be submitted.

General Go to **aisc.org/ej** for complete submittal instructions.

All papers within the scope outlined above will be reviewed by engineers selected from among AISC, industry, design firms, and universities. The standard review process includes outside review by an average of three reviewers, who are experts in their respective technical area, and volunteers in the program. Published papers become the property of the American Institute of Steel Construction and are protected by appropriate copyrights. No typesetting proofs will be provided to authors.

Manuscripts Manuscripts must be provided in Microsoft Word format. Include a PDF with your submittal so we may verify fonts, equations, and figures. View our complete author guidelines at **aisc.org/ej**.

Archives Search at **aisc.org/ej**. Article downloads are free.

Smarter. Stronger. Steel.

American Institute of Steel Construction
130 E Randolph St, Ste 2000, Chicago, IL 60601
312.670.2400 | aisc.org/ej